

# UC Davis

## UC Davis Electronic Theses and Dissertations

### Title

Demonstration of a digital twin of a laser ablated aluminum alloy 6061 disk for fault detection and process control.

### Permalink

<https://escholarship.org/uc/item/5mh206ch>

### Author

Matthews, Thomas

### Publication Date

2023

Peer reviewed|Thesis/dissertation

Demonstration of a digital twin of a laser ablated aluminum alloy 6061 disk for fault detection and process control.

By

THOMAS MATTHEWS  
THESIS

Submitted in partial satisfaction of the requirements for the degree of

MASTER OF SCIENCE

in

Mechanical and Aerospace Engineering

in the

OFFICE OF GRADUATE STUDIES

of the

UNIVERSITY OF CALIFORNIA

DAVIS

Approved:

---

Zhaodan Kong

---

Stephen K. Robinson

---

Barbara Linke

Committee in Charge

2023

## **Abstract**

With recent advances in computing, communication, sensor, and actuator technologies, it has become possible to create virtual representations of physical objects that can communicate with the real world. These connected virtual representations are a new technology, called digital twins, with the possibly to transform numerous industries including: manufacturing, aerospace, and medicine. While there are many examples of digital twins already, the current body of work is insufficient with the majority of the published work on digital twins featuring frameworks or demonstrations that lack the physical component. A set of functional digital twins of laser ablated disks are presented here to demonstrate how one can be used in a machining process. The virtual representations of the disks are a geometric model built in COMSOL Multiphysics<sup>®</sup> that defines the shape of the disk. The digital twins showcased are able to detect potential faults and control the ablation process. The fault detection was done using images of the plasma plumes generated during the process and modifications to the virtual representation were used to guide the amount of energy used by the laser ablation system to remove material from the physical disk's surface. In addition to demonstrating how the digital twins can be used as part of the process, three test cases are presented to display how the digital twins compared to their physical counterparts.

# Contents

- 1 Introduction** **1**
  
- 2 Background** **4**
  - 2.1 Digital Twins . . . . . 4
  - 2.2 Pre-Cursors to Digital Twins . . . . . 6
    - 2.2.1 Simulation and Modeling . . . . . 6
    - 2.2.2 Hardware-in-the-loop . . . . . 6
  - 2.3 Features of a digital Twin . . . . . 7
    - 2.3.1 Physical Entity . . . . . 7
    - 2.3.2 Virtual Representation . . . . . 7
    - 2.3.3 Physical to Virtual Connection . . . . . 7
    - 2.3.4 Virtual to Physical Connection . . . . . 8
    - 2.3.5 Fault Detection . . . . . 8
    - 2.3.6 Twinning Rate . . . . . 9
  - 2.4 Enabling Technology . . . . . 9
    - 2.4.1 Internet of Things . . . . . 9
    - 2.4.2 Cloud Computing . . . . . 10
  - 2.5 Digital Twin Applications . . . . . 10
    - 2.5.1 Automotive and Aerospace Industry . . . . . 10
    - 2.5.2 Medical Industry . . . . . 10
    - 2.5.3 Manufacturing . . . . . 11
    - 2.5.4 Facility Management . . . . . 13
  - 2.6 Open Challenges . . . . . 13
    - 2.6.1 Data Privacy and Security . . . . . 13
    - 2.6.2 Proprietary Applications . . . . . 13

2.6.3	Wealth Disparity . . . . .	14
2.7	Laser Machining . . . . .	14
2.7.1	Solid-State Lasers . . . . .	14
2.7.2	Flashlamps . . . . .	15
2.7.3	Q-switching . . . . .	15
2.7.4	Laser Ablation . . . . .	15
2.7.5	Plasma formation . . . . .	16
2.7.6	Modeling of Laser Ablation . . . . .	16
<b>3</b>	<b>Methodology</b>	<b>17</b>
3.1	Physical Entity . . . . .	18
3.1.1	Laser . . . . .	19
3.1.2	Delay Generator . . . . .	19
3.2	Virtual Representation . . . . .	20
3.2.1	3D Modeling . . . . .	20
3.2.2	2D Axi-Symmetric Modeling . . . . .	23
3.3	Physical-to-Virtual Connection . . . . .	27
3.4	Virtual-to-Physical Connection . . . . .	29
3.4.1	Process Control . . . . .	30
3.4.2	Fault Detection . . . . .	31
3.5	Digital Twin Application . . . . .	32
<b>4</b>	<b>Results</b>	<b>35</b>
4.1	Initial Attempts . . . . .	35
4.2	Fault Detection . . . . .	37
4.2.1	No Plume Detected . . . . .	38
4.2.2	Low Energy . . . . .	38
4.2.3	High Energy . . . . .	39
4.2.4	Depth Exceeded . . . . .	39
4.3	Physical Entity to Virtual Representation . . . . .	40
4.4	Discussion: Crater Depth Differences . . . . .	43
<b>5</b>	<b>Conclusion</b>	<b>45</b>
	<b>Appendix</b>	<b>48</b>



# List of Figures

- 2.1 Graph of digital twin publications as function of time with the category indicated by the color coding. Reprinted from Figure 2 of "Analyzing the Scholarly Literature of Digital Twin Research: Trends, Topics and Structure" by Emmert-Streib, Tripathi, and Dehmer [1], Copyright 2023, with permission from Frank Emmert-Streib . . . . . 5
- 2.2 The system diagram of a proposed digital twin of instruments for the purpose of fault diagnosis and prediction. Reprinted from Figure 1 of "Intelligent instrument fault diagnosis and prediction system based on digital twin technology" by Gao *et al.* [2], licensed under CC BY 3.0. . . . . 12
- 3.1 An overview of how the digital twin operates. The physical entity is a 6061 aluminum alloy disk, which will be ablated. During the ablation, an image of the plasma plume that forms is captured and used to extract the amount of energy deposited on the surface as part of the physical-to-virtual connection. The virtual representation of that 6061 aluminum alloy disk is updated using a COMSOL Multiphysics<sup>®</sup> simulation of the ablation process. Finally the virtual-to-physical connection provides fault detection of the ablation process and control over the transmission percentage of the laser. . . . . 18
- 3.2 A 6061 aluminum alloy disk prior to being used as the physical entity in a laser ablation experiment. . . . . 18
- 3.3 A diagram of the laser ablation system used to create the craters on the surfaces of the physical entities. . . . . 19

3.4	The laser ablation system used to ablate the physical entity. The Laser beam originates from the laser head in the center of the image. The beam then travels through two reflecting optics to reach the focusing optic and hits the surface which is mounted on the stage in the lower left corner of the image. To the right of the stage is a magnification lens and a band-pass filter which light generated by the plasma plume travels through before being imaged by the iCCD camera in the right of the image. . . . .	20
3.5	The COMSOL Multiphysics <sup>®</sup> user interface, also referred to as COMSOL Desktop <sup>®</sup> , which was used to create the virtual representation. The elements of the model are displayed in the left hand section. Parameter values of the model elements can viewed and edited in the center column and model elements can be viewed graphical in the right most section. . . . .	21
3.6	The three dimensional model displaying the heating of the aluminum target from the ray power being deposited on the surface. The beam begins at the bottom center of the image and travels to the right (along the positive x axis) towards the beam splitter cube, which is represented by the outline a cube. One percent of the light continues traveling to the right and is captured by the beam profile sensor, represented by a small disk. The remaining 99 percent of the light is reflected to travel upwards and to the left (along the y axis). The rays are focused by the lens, shown as an outline of a disk, onto the surface of the virtual representation of the aluminum alloy disk. The colorbar indicates the temperature scale of the target in degrees kelvin . . . . .	22
3.7	The indentation created in the surface's mesh using the moving mesh module, viewed in the COMSOL Multiphysics <sup>®</sup> user interface. The color represents different temperatures of the material, with lighter colors indicating higher temperatures caused by heating from the laser beam. . . . .	22
3.8	Views of the virtual representation in a 2D Axi-Symmetric model. The view is of the two dimensional description rotated about the central axis to express it in 3D dimensions. The colorbar on the right side of both images is the temperature in degrees kelvin . . . . .	23
3.9	The mesh elements of the virtual representation are much smaller at the top of the disk close to the central axis. The elements are much larger as they move away from the point of impact of the laser, since the laser heating will only affect the small area at the top of the disk near the central axis. . . . .	24



3.10	The plume of evaporated material formed during the laser ablation of an aluminum target with the bounds of the plume in red. The vertical line protruding out of the top and bottom of the plume is the surface that is being ablated. The light to right of the vertical line formed by the protrusions is the plasma plume, while the light to left of the vertical line is the plume's reflection off of the disk's surface. The image is taken using the optics and camera seen in Figure 3.4. . . . . .	28
3.11	The averaged plume widths and energy readings at each different laser transmission level. A fit to the data is given in Equation 3.11. . . . .	29
3.12	The relationship between the depth of the crater formed in simulation for a given energy value. The expression of the trend line is seen in Equation (3.12). . . . .	30
3.13	The relationship between the transmission percentage of the attenuator mounted on the laser and the energy with a pulse. The expression of the trend line is seen in Equation (3.13). . . .	31
3.14	The application used to control the equipment, collect the plume images, and run the COMSOL Multiphysics <sup>®</sup> simulations. The graph in the left hand section of the interface displays the triangular elements of the mesh and the window in the right hand section shows the image of the plume captured from the most recent laser pulse. . . . .	33
3.15	The block diagram of the LabVIEW <sup>™</sup> code that controls the laser ablation system, extracts the energy measurement, and interfaces with COMSOL Multiphysics <sup>®</sup> to update the virtual representation. . . . .	34
4.1	Depth profile of an ablation crater with jagged features rising upwards out of the crater. The colorbar in the lower left corner of the image indicates the depth, with positive values representing heights above the over flat surface. Darker colors indicate deeper locations of the crater. . . . .	35
4.2	The crater depth after multiple laser pulses have impacted the surface of the material with the attenuator set to thirty percent transmission. This amount of energy created a jagged surface with points reaching up out of the crater and would not match virtual representations. The jagged points were smoothed out after repeated pulses, however a raised mound remained in the center of the crater, as seen in the lower right image. . . . .	36
4.3	The crater depth after multiple laser pulses have impacted the surface of the material with the attenuator set to ten percent transmission. With lower energy levels the craters were much smoother and more closely resembled the craters formed on the virtual representations.	37

4.4	Camera images displaying the three fault conditions that can be determined using the plume imaging. The images display the side of the plume and the plume’s reflection in the surface of the disks. They were captured at the same horizontal position as the plume, from the plume’s right side. . . . .	38
4.5	Laser pulse with too much energy creates a vastly different and unpredictable surface that the virtual representation can not match. . . . .	39
4.6	The application dashboard alerting the user to the laser pulse containing more energy than expected. . . . .	40
4.7	The virtual representation of the surface and the optical profiler measurements of the physical surface for the 1 $\mu\text{m}$ test case. The average depth over the circle in (a) was 1.012 $\mu\text{m}$ . . . . .	41
4.8	The virtual representation of the surface and the optical profiler measurements of the physical surface for the 2 $\mu\text{m}$ test case. The average depth over the circle in (a) was 1.431 $\mu\text{m}$ . . . . .	42
4.9	The virtual representation of the surface and the optical profiler measurements of the physical surface for the 3 $\mu\text{m}$ test case. The average depth over the circle in (a) was 2.012 $\mu\text{m}$ . . . . .	42

# List of Tables

3.1	The reported ablation depth on the central axis and simulation time for an input energy of 15 mJ with varying maximum elements sizes for the mesh in the ablated region. The data was collected by performing the simulation with each of the maximum mesh element sizes listed and measuring the change in the mesh’s height along the central axis. . . . .	24
4.1	Comparison of the depths of the craters on the physical entities and the virtual representations.	41
A.1	The plume width data collected as part of the data set used to determine the plume width to pulse energy relationship. . . . .	48
A.2	The pulse energy data collected as part of the data set used to determine the plume width to pulse energy relationship. . . . .	49
A.3	The depths of the craters formed in the COMSOL Multiphysics® simulation for different energy inputs. . . . .	50
A.4	Parameters used in the COMSOL Multiphysics® model. . . . .	51

# Chapter 1

## Introduction

The advancement of the capabilities of manufacturing has been an essential part of the technological advancement of humans, with the earliest known use of machining dating back to the Roman Empire [3]. The development of new technologies has happened in lockstep with the development of more precise and sophisticated components. This effect was apparent during the first industrial revolution, from 1760 to 1830. James Watt's steam engine required cast iron and copper alloy parts, which could not be produced with enough precision by hand. To overcome this, John Wilkinson invented a water powered boring machine, which is widely regarded as the first modern machine tool [4]. This machine was capable of boring a hole to within one sixteenth of an inch of the desired diameter [5]. With the ability to mass produce the parts needed for steam engines, steam power became more accessible. This spurred the rapid development of the machines powering the industrial revolution. With reliable consistency of produced parts, it was not long before the first replaceable parts appeared. Eli Whitney tasked with producing 10,000 muskets for the U.S. military, had the necessary parts machined such that any set of the individual parts could be assembled into a rifle [6]. He proved this capability by disassembling the rifles and reassembling them with randomly chosen parts in front of the United States Congress [5].

From the early 20th century through to the end of the Second World War, machine tools were heavily used in the automobile and aircraft manufacturing industries in the United States [7]. The capabilities of machining continued to grow leading to the creation of Ultra-Precision Machining technologies [8] after the Second World War, and computerized numerical control (CNC) machines in the late 1960s [9]. Computer aided design (CAD) software also improved the efficiency of manufacturing processes by enabling direct interfacing between machine tools and the computers used to design the parts being fabricated [7].

Today we are experiencing the fourth industrial revolution, where the role of computerized systems to

collect, store, and use data has grown dramatically. Sensors have gotten smaller and more energy efficient, allowing them to be incorporated into more devices than ever before. The ability to collect and process large amounts of data is enabling a new technology, digital twins. Digital twins are an emerging technology which has applications in a variety of fields [10]. It is broadly defined as a virtual representation of a physical entity with communication between the virtual and physical domains [11]. These virtual representations are descriptions of the physical entities they correspond to in a digital environment. In the context of manufacturing digital twins could be utilized in a variety of ways, as the production facilities, equipment, or items being produced. Using sensors, both onboard the production equipment and external, the status of manufacturing processes can be monitored and used to update the virtual representation of a digital twin of a product as it is manufactured. Digital twins of products can be utilized both during the manufacturing and its operational life. As a product moves towards completion, its digital twin can be used to monitor processes and detect defects. In addition to the benefits during manufacturing, the digital twins can incorporate any inspection or quality assurance data collected for use by the customers.

This research sets out to create and test the construction of digital twins of machined parts made using a nanosecond laser ablation system to perform laser drilling. Laser drilling is a machining technique with the capability to drill holes with diameters between 0.005 mm and 1.5 mm and depth to diameter ratios between 1 and 50 [12], making it useful for the machining of aircraft parts and electronics [13]. The small scale of the holes created by laser drilling and the frequent need for precision, makes parts machined with laser drilling an interesting candidate for digital twins and a likely use case for industry in the future. By creating a virtual representation of the part during machining, system operators can view a prediction of the resulting changes to the part without the use of measurement equipment. Digital twins of laser drilling equipment [14] and the parts produced with laser drilling [15], have already been proposed in literature. The digital twin proposed by Stavropoulos, Papacharalampopoulos, and Athanasopoulou used a model of a femtosecond laser pulse to remove material, which is modeled differently from nanosecond and longer laser pulses. Their work also did not consider the time required to simulate the change to the part. The research presented here aims to expand the existing research for laser drilling digital twins by contributing a working example of a digital twin of a part machined using nanosecond laser pulses while operating within the time and resource constraints needed for real-time usage in industry.

Just as previous advances in manufacturing capabilities have improved the technological capabilities of humanity, digital twins offer the same opportunity. The development of digital twins promises to benefit both manufacturers and consumers. By allowing manufacturers to track virtual representations of their products, they can monitor trends and identify faults, both during and after production. For consumers, digital twins offer a variety of benefits from predictive maintenance [16] to system optimization [17]. However none of

these advantages can be utilized without methodologies for manufacturers to build their own digital twin systems from. To provide these methodologies it is important that research is performed on a wide variety of techniques and applications for digital twins, so that system designers have examples that fit their unique production systems.

## Research Objective

The purpose of this project is to demonstrate how digital twins can be used in a machining process, by creating digital twins of parts being laser machined. To facilitate the laser machining a standard laser ablation system was used to create small craters on the surfaces of the parts. These craters were made to provide a removal of material similar to the effects of laser drilling. To provide information of the machining process to the virtual representations of the part, an intensified charge coupled device (iCCD) camera was used to image the plasma plumes generated by the removal of material. This provided both a means of observing the plumes generated to detect potential faults and measurements of the energy deposited on the surfaces of the parts, which was used as an input to a simulation of the laser ablation process. After adjusting for this input the virtual representation could be used as a prediction of the physical crater's depth and the amount of ablation still required. These elements were combined to create a connected set of physical entities and virtual representations that drove a feedback loop to control the machining process.

While this effort is only a small portion of the on-going work of the fourth industrial revolution, the usage of digital twins during manufacturing holds great potential for manufacturers. By monitoring both a physical part and its virtual representation as it is built or machined, manufacturers can compare the two. This data can be used to provide insights to guide the manufacturing processes, as described below, or be used to identify artifacts, systemic issues, and inefficiencies of the production process. Through the incorporation of digital twins, manufacturers can leverage the volumes of data that are now accessible with modern sensors to improve their efficiency and precision.

# Chapter 2

## Background

### 2.1 Digital Twins

The concept of digital twins was first presented by Michael Grieves in 2002 at a product life-cycle management conference [18]. Over the next decade and a half interest in digital twins grew slowly, with a recent boom in the number of publications about digital twins and their potential [11, 10, 1], shown in Figure 2.1. The growing interest has caught the attention of not just those in academia, but also industry keen to apply this new technology. In particular, Siemens has been actively involved in developing tools for applying the digital twin concept [19, 20] and even holds patents on multiple digital twin related inventions [21].

While exact definitions of what a digital twin is vary [22], the consensus formed in literature is that a digital twin is a virtual representation of a physical entity with bidirectional-communication between the virtual and real space [10, 23, 24]. By integrating these components together the digital twin can create a process where information is collected from the physical entity and used to update the virtual representation. The virtual representation can then in turn create some insight to be communicated back to the physical system to be leveraged in the real world. This process serves as a feedback loop to provide numerous benefits to the system operators and designers. This concept is similar to that of digital shadows, which are virtual representations of real world objects and receive real world data to stay up to date [25]. In contrast to a digital twin, digital shadows exist as just the virtual representations and contain no models, simulations, or other means of utilizing the physical entity's data beyond viewing the assigned status.

A digital twin should not be confused with a simulation either. The essential difference between a digital twin and simulation is the connection between the virtual representation and the physical entity. Without that flow of information the simulation is a representation of a physical entity as it was at the time of

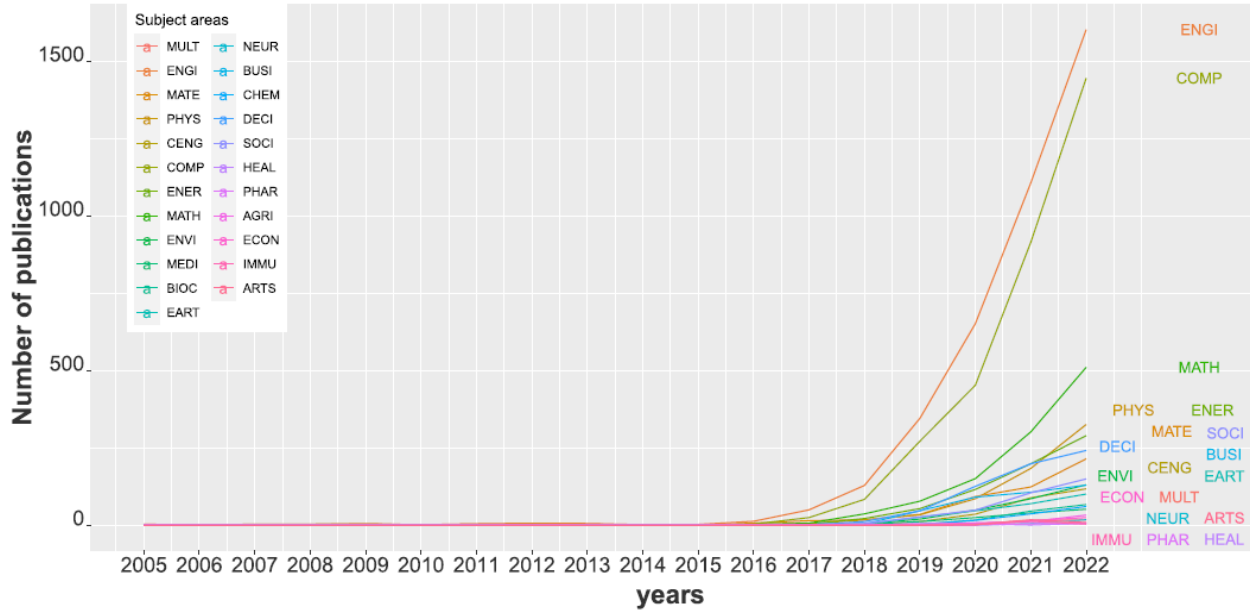


Figure 2.1: Graph of digital twin publications as function of time with the category indicated by the color coding. Reprinted from Figure 2 of "Analyzing the Scholarly Literature of Digital Twin Research: Trends, Topics and Structure" by Emmert-Streib, Tripathi, and Dehmer [1], Copyright 2023, with permission from Frank Emmert-Streib

measurement. Over time the differences between the simulation and the physical entity will grow, since there is no information being feed to the simulation to keep it in sync. That is not to say a simulation cannot be a part of a digital twin, simulations can be leveraged by a digital twin to use measured data and predict a physical process or property.

Once a digital twin is created and is linked to its physical entity, it is intended to remain connected to the physical entity as an inseparable pair for the rest of its operational lifespan. There are suggestions in literature that digital twins should be created during the manufacturing process, so that any initialization or quality assurance data can be incorporated in the digital twin prior to the use of its physical entity [26]. In doing so vendors could provide digital twins of their products to manufacturers who could incorporate them as components in a digital twin of a larger product, creating a digital twin out of smaller digital twins. While potentially beneficial to system designers, this could increase the development effort if there are not industry standards to define how digital twins interface with each other.

One advantage to the system designer is the ability to collect performance data for a product throughout its life cycle. This would enable engineers to evaluate how the product performs in different environments, and make adjustments to the product in the current production cycle instead of in the next iteration of the product [27].



## 2.2 Pre-Cursors to Digital Twins

Like most innovations, digital twins are an improvement on existing methods. There are numerous methodologies used in industry that incorporate a subset of the features that make a digital twin, some which are outlined in the following sections.

### 2.2.1 Simulation and Modeling

As noted earlier simulations are only a part of digital twins, however the development of simulations and computational models was a necessary step in the technological advancement towards digital twins. The first computerized simulation was the usage of the Monte Carlo method at Los Alamos Laboratory on the newly built Electric Numerical Integrator and Computer (ENIAC) [28]. Since then the availability of computational power has grown, as Gordon Moore famously predicted in 1975 [29], in what is called Moore’s Law. This prediction has held true until at least 2020 [30], however it may soon be no longer be true as the semiconductor industry shifts from reducing the size of components to reducing energy consumption [31]. With this growth in computational power the number of simulation tools has grown as well, resulting in 137 simulation programming languages being created by 1981 [32]. Today there are many different tools available for simulating a broad spectrum of physical systems [33]. For this research, COMSOL Multiphysics<sup>®</sup>, a commercially available simulation environment, is used for the simulations.

### 2.2.2 Hardware-in-the-loop

Another step closer to digital twins was the application of simulations outside of an isolated digital environment, hardware-in-the-loop. This method enables system designers to test their control algorithms on the hardware that will be used. The controller under test communicates with a simulated version of the system that will be controlled [34]. The interaction between the hardware and the simulation acts in a similar fashion to a digital twin’s connections to the real world. However instead of using the virtual representation to generate information for the betterment of the corresponding physical entity, the hardware-in-the-loop’s simulation merely provides a simulated response to the controller’s output. While this may seem similar to a digital twin, it is important to note that the simulation does not represent the hardware being tested. Additionally, the hardware-in-the-loop is used solely during the development stages of a controller and digital twins are intended to exist throughout a system’s lifespan. However, hardware-in-the-loop testing can be improved through the usage of digital twins. In this use case the simulated system that interacts with the controller under test is a digital twin of the system [35]. The digital twin used in this paradigm could be either the “pre-digital twin” that Makarov *et al.* define as the virtual prototype during product development

[36] or a digital twin of a system already in operation when evaluating new components.

## **2.3 Features of a digital Twin**

As explained above, there are a number of elements required for a digital twin. Most important is the linkage between the virtual representation and the physical entity.

### **2.3.1 Physical Entity**

The available literature does not place any bounds on what a digital twin can be created for. However the examples seen in literature tend to focus on manufacturing, aerospace, and medical applications [10]. These industries are interested in the development of digital twin technology due to both the improvements to human safety and the reduction in monetary cost that predicting, detecting, and diagnosing problems provides.

### **2.3.2 Virtual Representation**

The virtual representation can be any digital expression of the system that is able to create an accurate depiction of the state of the system. The form of the virtual representation is heavily dependent on the physical entity and the purpose behind creating a digital twin. Some examples from literature include using a geometric description for a machined part [37], a state space model for a solar farm [17], and a machine learning model for petrochemical production control [38]. Regardless of how the virtual presentation captures the physical entity, a clear consensus is formed in literature that the virtual representation must be of high fidelity [11, 21, 39]. This requirement is derived from the fact that digital twins are not designed to be a model of an object's specifications, but the virtual representation of a singular instance of the object. As such, the virtual representation must capture the individual features of its physical entity. To properly describe the physical entity, the virtual representation must be able to change according to changes in the physical entity over its lifespan.

### **2.3.3 Physical to Virtual Connection**

In order for the virtual representation to satisfy the high fidelity requirement the state of the physical entity must be communicated to the virtual representation [40]. This information can be gathered in a variety of different ways, but a common approach is using sensors on or in the physical entity [16]. The ability to incorporate sensors into the physical entity has become easier thanks to the development of micro-electro-

mechanical systems (MEMS) sensors [41]. While MEMS sensors are currently not used in machine tools, they can be utilized in products to acquire data for the product’s digital twin. The small form factor of MEMS sensors makes them easy to fit into a system, and their low power usage means that it is possible for them to operate on battery power alone for the duration of the system’s working life [26] depending on its lifespan. MEMS sensors have already been demonstrated for usage in digital twin applications [42].

In the event that the virtual representation is not stored locally, the sensor data will need to be communicated to the remote server that houses the virtual representation. Fortunately the deployment of 5G networks has enabled high speed, low latency wireless data transmissions [43].

### **2.3.4 Virtual to Physical Connection**

The focus of the communication from the virtual representation to the physical entity usually is to provide some information that can be acted upon to enhance the operations of the physical entity. As with the other components of a digital twin, it can take many forms and is typically determined based on what best suits the application. In the solar farm example mentioned earlier, the optimized power factor set points were communicated to the system to maximize output while staying within safety margins [17]. Another common form of insight is fault prediction, detection, and diagnosis information [24]. This use case is of particular interest to the aerospace industry. Increased forecasting of failures would allow aircraft operators to schedule maintenance more effectively and reduce downtime of their aircraft [16].

### **2.3.5 Fault Detection**

There are many methods of fault detection developed for different applications today [44]. These methods range in both the amount of expert knowledge required to identify faults and the complexity of the mathematics used in the fault detection algorithms. The continuous collection of sensor data from a digital twin’s physical entity provides a natural opportunity to incorporate fault detection into many digital twin systems.

One such example utilized key performance indicators (KPIs) from the aggregation of sensor data to monitor the health of a system [45]. A linear regression of the KPIs would reveal trends in the performance data without the need for training models or expert knowledge. Thresholds could then be set to alarm the human operators when a fault would occur.

More complicated approaches to fault detection have also been presented in literature. Neural networks have been developed for usage in proposed digital twins [46, 47]. Darvishi, Eivind, and Rossi proposed a machine learning architecture to detect and isolate faults in the Internet of Things (IoT) sensors on board a digital twin’s physical entity. Their methodology entailed creating a machine learning model which produced

virtual sensor readings that could be compared to the real sensor output. The residual of real and virtual readings were then used as inputs to a neural network classifier to isolate the sensor in which the fault occurred. With the faulty sensors identified, the virtual sensor readings could be used in place of the failed real sensors. Similarly, Wang *et al.* [46] put forward a digital twin that utilized XGBoost to create a fault classifier. After training the model on existing optical communications data, the model was able to detect faults in the network one day prior to failure occurring.

### 2.3.6 Twinning Rate

The synchronization between physical entity and virtual representation is referred to as twinning. The rate at which this synchronization takes place is described in literature as a process happening constantly in real time [11]. Under this paradigm, the onboard sensors in the physical entity would be continuously collecting and transmitting data to the virtual representation with any adjustment made in the virtual representation realized instantly in the physical entity. This would ensure the high fidelity requirement of keeping the virtual representation as an up-to-date description of the physical entity. However certain information cannot be communicated in real time, as Detzner and Eigner [27] illustrate with their example discussing vehicle maintenance data. The repair and replacement of components within a vehicle would not be detected by the vehicle's sensors, thus requiring manual entry of the operations performed. The synchronization of the physical entity and virtual representation would take place after the maintenance was completed, not in real time.

## 2.4 Enabling Technology

At the time of digital twin's initial inception the technology required to gather, communicate, and utilize the information needed was not available. A digital twin created at that time would have limited functionality. Over the past twenty years there have been large advancements in the technological capabilities of sensors and digital communications [21], which now make achieving digital twin's technological requirements feasible.

### 2.4.1 Internet of Things

The operation of many digital twins will require that the physical entity's onboard sensors and actuators be able to communicate with other devices. The Internet of Things (IoT) provides the infrastructure for device to device communication via the internet [48]. This connectivity enables devices to work together remotely to accomplish a shared task [49]. When applied to digital twins, the virtual representation can receive data and provide feedback to the physical entity regardless of the physical location of either component.

## 2.4.2 Cloud Computing

Without the need to store the virtual representation locally, it could be kept in a cloud based environment. For digital twin applications that are highly mobile, such as vehicles, or those that cannot house the computation equipment to store and run the virtual representation, such as medical applications, cloud based environments offer a location for the virtual representation to exist [50]. The remote nature of cloud systems also adds the benefit of allowing access to the virtual representation for multiple users of the data. For healthcare applications the remote access will be particularly important as it allows for healthcare providers to access patient data for diagnosis and treatment planning [51].

## 2.5 Digital Twin Applications

As interest in digital twins has grown, the literature has focused on applications within a small number of industries [10].

### 2.5.1 Automotive and Aerospace Industry

The recent increase in the availability and affordability of IoT sensors has enabled automotive and aircraft manufacturers to use embedded sensors for monitoring a wide range of parameters. This provides the vehicles with the operational conditions of its sub-systems. The main incentive for the adoption of digital twins within the aerospace industry is the benefit of fault prediction [10] and degradation modeling [16]. Earlier warning of faults allows aircraft operators to schedule the maintenance required for opportune times rather than causing costly delays. While full scale digital twins of aircraft have not been developed yet, digital twins of plane subsystems have been created [16].

The automotive industry is interested in utilizing digital twins for more than just preventive maintenance. Since automobiles are used in a wide variety of environments the degradation of components cannot always be predicted. The digital twins of automobiles can be used by engineers both during their operational life and afterwards to evaluate the state of automobiles after being deployed in a variety of different environments [27].

### 2.5.2 Medical Industry

The development of digital twins for medical applications could provide many advantages to patient care. With medical devices becoming more sophisticated the amount of health data that can be collected about an individual has increased. Through the usage of Wireless Body Area Networks (WBAN), sensor data from

medical devices can be collected and sent through the internet [52]. This data along with data gathered by a patient’s healthcare providers can be used to create a virtual representation of the patient.

As data is fed to the digital twin, mathematical models of the human body can be used to screen for potential illnesses and create personalized models for treatment [53]. Already digital twins have been tested for the treatment of type 1 diabetes [54]. Using blood glucose readings collected during an initial period with a generic closed loop model, digital twins were created for each patient to model their blood glucose levels.

As with much of today’s storage of patient healthcare information, healthcare digital twins will likely be stored in a cloud environment. This will allow healthcare providers to access patient data more easily. Their ease of access will be useful not only in the treatment of patients, but also in the allocation and planning of healthcare resources (hospital beds, staffing, etc.) [51]. In addition to the potential benefits of using patient data in cloud based digital twins, there is also the difficulty of implementing a system compliant with the Health Insurance Portability and Accountability Act (HIPAA) and the added risk of potential data breaches of private medical information.

### **2.5.3 Manufacturing**

Digital twins have always been discussed as a product life-cycle management technology, however 43.3% of the available literature as of 2020 is focused on just the manufacturing stage of products [55]. Given this, it is unsurprising that manufacturing applications have the largest representation among the digital twins proposed so far [10]. The scale of digital twins proposed in literature cover all aspects of production including the production facility [56], the production equipment [57], and the products themselves [37].

The introduction of automated manufacturing equipment, such as CNC machines, has increased the productivity of manufacturing industries [9]. Continuing this trend, there are efforts to leverage the wealth of data that can be collected during factory operations to track, analyze, and optimize the performance of facilities [56]. To do so, the data of products, employees, and equipment must be collected and processed. Several strategies have already been proposed including ticket based tracking methods [58], and location sensors to track both employee and product movements [59]. In Figure 2.2, a digital twin of factory equipment for the purpose of fault detection is illustrated. Collected data is only part of the effort required in the development of digital twins, a virtual representation must also be created to utilize the data. Fortunately there are existing tools that can be used to create virtual representations of factories. Siemens Tecnomatix plant simulator has been used in multiple digital twin demonstrations to create a virtual representation [26, 59]. To complete the facility level digital twins, a virtual-to-physical connection is required. This

virtual-to-physical connection often takes the form of an optimization of the production facility’s workflow to improve efficiency or throughput [56]. Digital twins of the machine tools within factories are also a topic of interest. As machine tools have become more sophisticated, they have become increasingly computerized. The connectivity and data collection offered by modern machine tools make them ideal candidates for the adoption of digital twins. There has already been effort put into the conceptualization of digital twins for CNC machine tools [57]. In the ultra precision machining field, digital twins could be beneficial in both fault detection and reducing processing time during the planing of part machining [8].

Beyond just the factories and the machines, the parts being produced are another possible application of digital twins. As products are created, it has been suggested their digital twins should be produced along side them [60]. Under this paradigm as parts are being manufactured, the operations would be performed in both the physical world and the virtual environment. This process would allow for the deviations or defects as a result of the manufacturing process to be detected. Additionally vendors could supply the digital twins

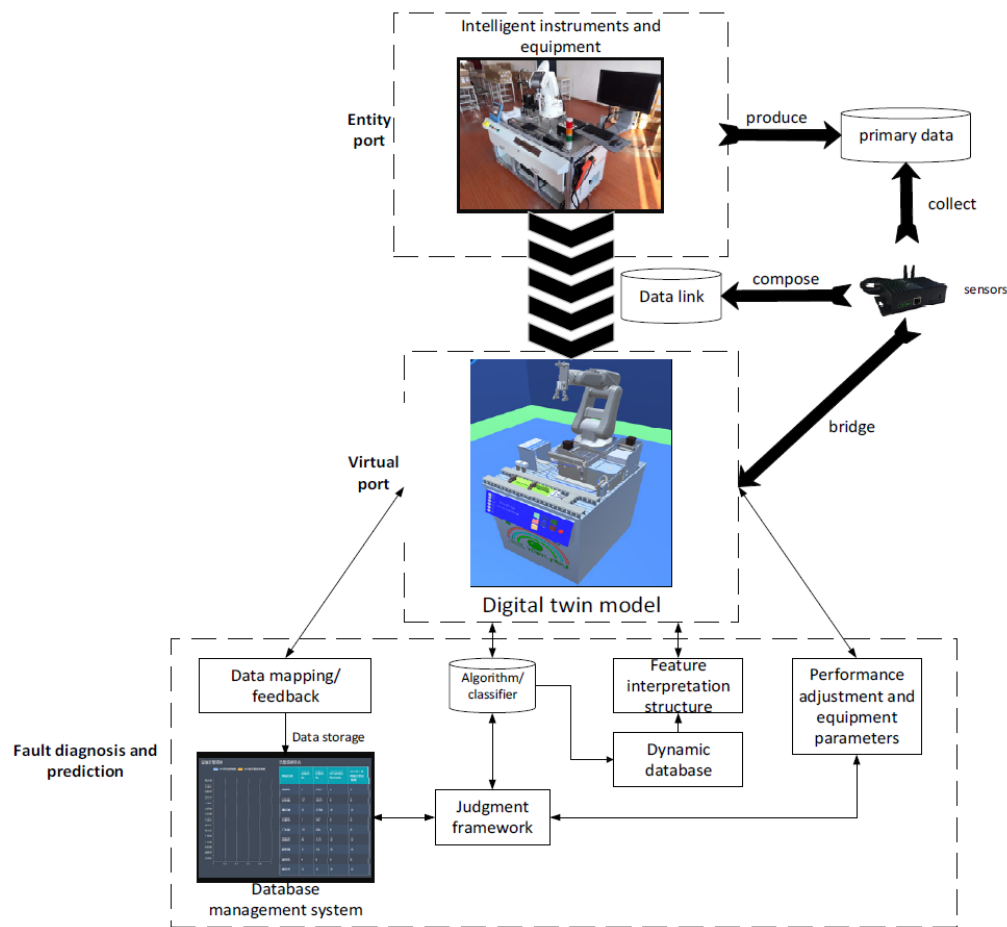


Figure 2.2: The system diagram of a proposed digital twin of instruments for the purpose of fault diagnosis and prediction. Reprinted from Figure 1 of "Intelligent instrument fault diagnosis and prediction system based on digital twin technology" by Gao *et al.* [2], licensed under CC BY 3.0.

of their products to customers to be used in larger digital twins [19].

The scale of digital twins proposed for manufacturing varies from whole factories down to individual parts being produced. Adoption of these different levels of digital twins is not intended to be exclusive to one another. On the contrary, it is suggested that to fully benefit from digitization, manufacturers should seek to create a digital twin factory which houses the virtual representations of their equipment and of the products progressing through their factory [26].

#### **2.5.4 Facility Management**

Interest in facility level digital twins is not limited to just production facilities. Xie *et al.* [61] demonstrated a digital twin of the Institute for Manufacturing at the University of Cambridge. By using historical vibration data from the building’s variable refrigerant flow cooling pumps, they were able to detect faults that would adversely effect the systems regulating the building’s temperature.

There are also efforts to develop digital twins of buildings on smaller scales [62]. Lydon *et al.* used simulations of the thermal properties of a concrete roof to determine placement of hydronic piping. Once determined, a digital twin of the building was used to develop the control policy of the heating system.

### **2.6 Open Challenges**

Digital twins have huge potential benefits to the operators and designers of systems, however there are still many unaddressed issues surrounding the topic [10, 63].

#### **2.6.1 Data Privacy and Security**

As with any digital system, there is concern over the data collected by digital twins. Cybercrime is a large problem in today’s connected world that is expected to continue growing [64]. The large volumes of data that digital twins will collect combined with the likelihood of them being accessible through the internet will make them an appealing target to criminals. Potential data breaches have already started to happen. Siemens Metaverse, a platform for the creation of digital twins of factories and offices, was discovered in March of 2023 to have leaked user credentials of another application owned by Siemens, ComfyApp [65].

#### **2.6.2 Proprietary Applications**

In order for a digital twin to communicate with other digital twins, its developers must create an interface through which it can send and receive data. Since digital twins are still an emerging technology, there is



currently no definition of how digital twins should communicate with one another. This could pose a large risk to the ability to use digital twins from multiple vendors due to the difficulty of supporting multiple standards. To alleviate this and enhance the potential benefit of digital twins, industry standards must be created for how digital twins communicate with each other.

The usage of proprietary technologies could also increase the cost of using digital twins and limit access to only applications with large budgets. That does not mean that it is impossible to create a digital twin without using licensed proprietary tools. Karan *et al.* [66] proved this by making a digital twin using free and open source tools.

### 2.6.3 Wealth Disparity

Digital twins will likely be costly due to the large amount of resources needed to develop and support them. The economic burden will most likely exclude poorer individuals from the benefits of digital twins. This impact will be felt more strongly in the healthcare industry, where economic inequality already effects the quality of care received [10].

## 2.7 Laser Machining

Up to this point the background has covered digital twins. As discussed above, the application of a digital twin heavily influences its design. For that reason it is important to also provide background on lasers and laser ablation, which was used to machine the physical entities discussed in the later chapters and was simulated in the digital twins created.

### 2.7.1 Solid-State Lasers

Laser is an acronym for Light Amplification by the Stimulated Emission of Radiation, which describes the underlying physics of how they function. The basic operating principle of lasers is the creation of photons as a result of electrons decaying from an excited state into a ground state [67]. This process can happen spontaneously or as the result of a photon colliding with an electron in an excited state, this is called stimulated emission. Lasers use three major components to exploit this phenomenon and produce a beam: a gain medium, a source of energy, and an optical resonator [68]. The gain medium provides the amplification of the light needed to produce a laser beam [69]. Solid-state lasers are built using a solid material for the gain medium [70], as opposed to gas or liquid [68]. Yttrium aluminum garnet (YAG) is a crystal commonly used in gain mediums [71] due to its high optical transparency [72], low internal stress, high hardness, and

high thermal and chemical resistance [73, 74]. By themselves YAG crystals do not provide any amplification, however when they are doped with rare-earth ions they become active mediums [72].

### **2.7.2 Flashlamps**

To move electrons from the ground state to the excited state, frequently referred to as ‘pumping’ [67], a source of energy is required. As the electrons in the gain medium absorb energy eventually the majority of them will be in the excited state, this is called population inversion. This condition is necessary to produce enough photons to form a beam. Flashlamps were used in the first functioning laser in 1960 as the energy source [75]. They provide broad spectrum light of which only a small amount is absorbed by electrons in the gain medium, making them largely inefficient [76]. However despite this they still provide enough energy to cause population inversion and are used in many laser systems today. Other possible energy sources include electric currents or discharge, chemical reactions, and light produced by other lasers [68].

### **2.7.3 Q-switching**

As the photons are produced from spontaneous emission, it is necessary to confine those traveling along the axis of the gain medium to produce a beam. This is done using an optical resonator that will trap photons in an optical cavity. A simple example of this is two parallel mirrors, with one reflecting all light and the other being partially reflective to allow some the photons to escape and form the laser beam [70]. As the photons travel back and forth in the medium they will collide with excited electrons to produce more photons traveling in the same direction. This grows until enough photons are present that the amount escaping the cavity will produce a beam.

To increase the number of photons in a laser pulse, the loss of the resonator can be manipulated with a technique called Q-switching. This is done by adjusting the ratio of energy kept in the resonator to the energy loss per cycle, called the quality factor or Q [77]. By keeping cavity Q low, the formation of a beam will be prevented by the high losses in the gain medium. As the flashlamp pumps the electrons in the gain medium a higher level of population inversion will be reached. The Q is then raised to prevent loss in the gain medium, which prevents photons from leaving the medium. Finally the energy stored in the medium is converted into photons using stimulated emission and a high energy laser pulse is generated.

### **2.7.4 Laser Ablation**

Laser ablation is the process of removing material from a surface by depositing energy from a pulsed or continuous laser source. The time span of the pulses range between the femtoseconds and nanoseconds range

typically. The primary cause of the material removal is determined by the time span and the irradiance of the laser pulse [78]. For pulses in the femtoseconds range with an irradiance between  $10^{12}$  and  $10^{17}$  W/cm<sup>2</sup> most of the material removal is caused by Coulomb explosion, which is the phenomenon caused by the electrons absorbing energy and being ejected [79]. This creates a strong electric field in the material that repels the ions with a greater force than the binding energy of the lattice. Longer pulses in the nanosecond range with an irradiance ranging from  $10^7$  and  $10^{11}$  W/cm<sup>2</sup>, instead drive the removal of material through thermal vaporization.

### **2.7.5 Plasma formation**

Once the pulse has deposited its energy on the surface, a plasma plume is formed from the ejected material. The expansion of this plume is influenced by the environment in which the laser ablation is occurring. In a vacuum the expansion can be modeled using hydrodynamic equations [78] or Monte Carlo simulations [80]. When the plume is in a gas at ambient pressure the expansion of the plume and its interaction with the surrounding media can be modeled with one of several models [81, 82, 83], which define an expanding spherical shell.

The light produced by the plasma plume can be used in laser induced breakdown spectroscopy (LIBS) to determine the atomic composition of the material.

### **2.7.6 Modeling of Laser Ablation**

Due to differences in the prevailing phenomena as a result of time span and irradiance of the laser pulse, the methods employed in modeling the process depends on the timescale of the laser pulse. A common modeling approach used for the simulation of femtosecond and picosecond pulses is the two temperature model [84, 85, 86, 87], which considers the temperature of the lattice and of the electrons. For longer nanosecond pulse laser ablation, where the physics revolves more around the heating and vaporization of material, multiphysics simulations packages have been used to simulate the process of laser ablation with many leveraging modules that compute the thermodynamics, fluid flow, and change in geometry [88, 89, 90]. First principles models have also been used for both femtosecond and nanosecond pulses [91, 92, 93].

In addition to modeling the physics, machine learning models have been developed and trained to infer the surface of a material after laser ablation [94, 95]. A trained model can provide a prediction that closely matches the actual surface, however they must be trained for each material used [94].

# Chapter 3

## Methodology

The existing research on digital twins for usage in the manufacturing industry currently has an insufficient number of examples of digital twins being created and used during manufacturing. The majority of the work for manufacturing applications focuses on digital twins of the production facilities or equipment. While examples of digital twins of items being produced do exist [26], more research is needed into this application of digital twins; and this research endeavors to add a new use case to the body of research. Given the wide variety of machining techniques in use in industry today, it is necessary to create a large body of frameworks that those in industry can utilize in their own digital twin designs. The methodology presented below will serve as an example for how digital twins can be implemented in laser machining facilities for laser drilled components. It will ultimately contribute to the larger body of work required to make digital twins feasible for industrial usage.

For this project the digital twin concept was applied to a part being machined through laser drilling. A laser ablation system was used to remove material from the target by heating the surface up to the temperature at which the material boils and is ejected as a plasma plume. The virtual representation of the machined part is a geometric description defined in the mesh format used by COMSOL Multiphysics<sup>®</sup>. To update the virtual representation the plume that forms during laser ablation is imaged and analyzed to determine the input energy. That energy value is used in the ablation simulation, which keeps the digital twin in sync with its physical entity. The crater depth is determined from the shape of the crater formed in the virtual representation and used to evaluate the amount of energy to be used in the next laser pulse. The process continues in loop, as displayed in Figure 3.1, until the desired depth is reached. This method allows for the ablated depth to be estimated without the usage of other measurement techniques, which might require movement of the part [96]. Fault detection is performed using the plume images to determine if the

energy deviates from the expected value and alert the operator if the geometry might not be as expected.

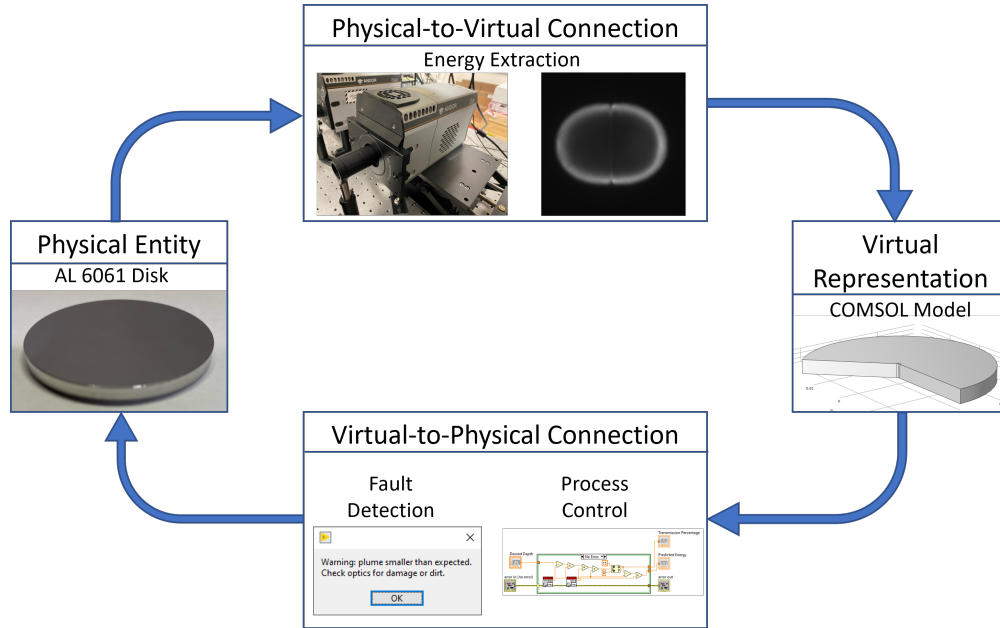


Figure 3.1: An overview of how the digital twin operates. The physical entity is a 6061 aluminum alloy disk, which will be ablated. During the ablation, an image of the plasma plume that forms is captured and used to extract the amount of energy deposited on the surface as part of the physical-to-virtual connection. The virtual representation of that 6061 aluminum alloy disk is updated using a COMSOL Multiphysics® simulation of the ablation process. Finally the virtual-to-physical connection provides fault detection of the ablation process and control over the transmission percentage of the laser.

### 3.1 Physical Entity

The physical entities, which the digital twins mirror, are disks of 6061 aluminum alloy, seen in Figure 3.2. The disks had a radius of 2 cm and thickness of 3 mm. The surface of the disks had a polished finish to create a smooth surface. This material was selected because of the usage of aluminum and its alloys in high precision aircraft components [97], which can require laser drilling to produce [98].

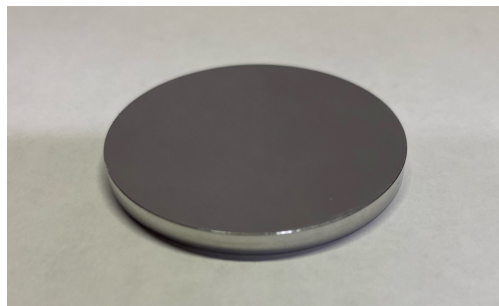


Figure 3.2: A 6061 aluminum alloy disk prior to being used as the physical entity in a laser ablation experiment.

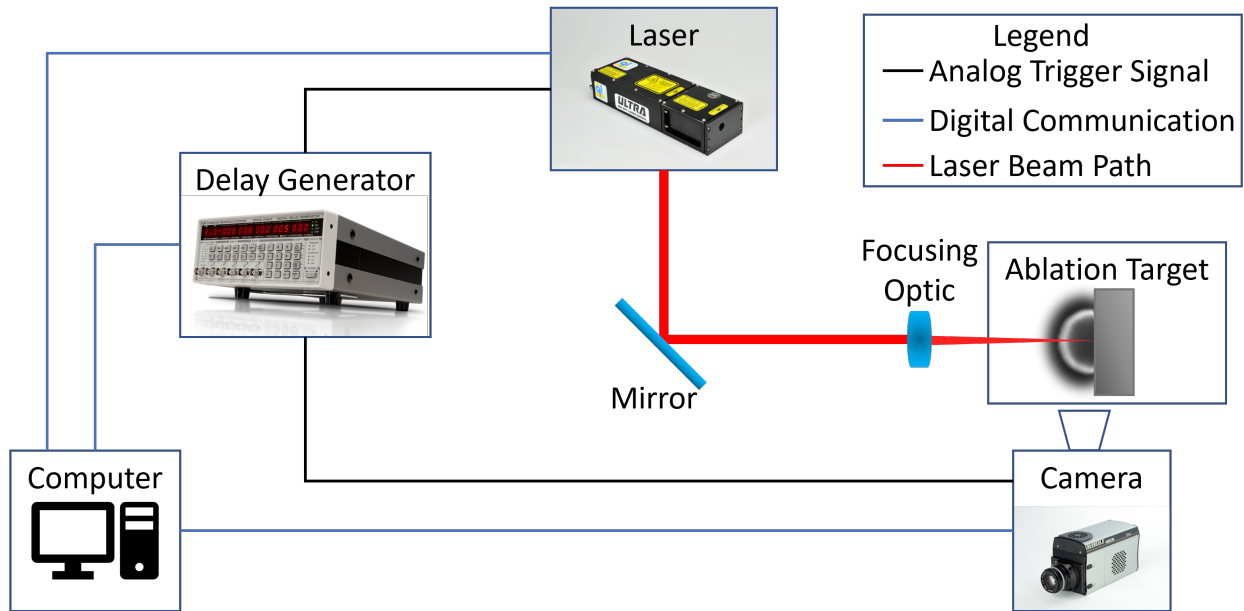


Figure 3.3: A diagram of the laser ablation system used to create the craters on the surfaces of the physical entities.

To perform the material removal a laser ablation system, pictured in 3.4, was used to deposit energy to the surface of the physical entity. The laser ablation system used a laser, a delay generator, and various optics to direct the light and focus it onto the surface of the physical entity, as depicted in Figure 3.3.

### 3.1.1 Laser

A Quantel Ultra 100, Q-Switched Nd:YAG laser that produced 1064 nm wavelength light was used. The laser was used in a single shot configuration to allow for the digital twin to perform the simulations between pulses. In order to control the amount of energy being deposited on the surface, a motorized variable attenuator (MVAT) was mounted on the output of the Quantel Ultra 100.

### 3.1.2 Delay Generator

A delay generator was used to control the timing of the laser and plume imaging camera to reduce the jitter in the system timing. The particular delay generator was a Stanford Research Systems DG645. Two of the DG645's outputs were used to trigger the flashlamp, the Q-switch, and the camera. The flashlamp and the camera were triggered by the first output and the Q-switch was triggered by the second. The camera used its own internal delay as well to make adjusting the shutter timing easier.

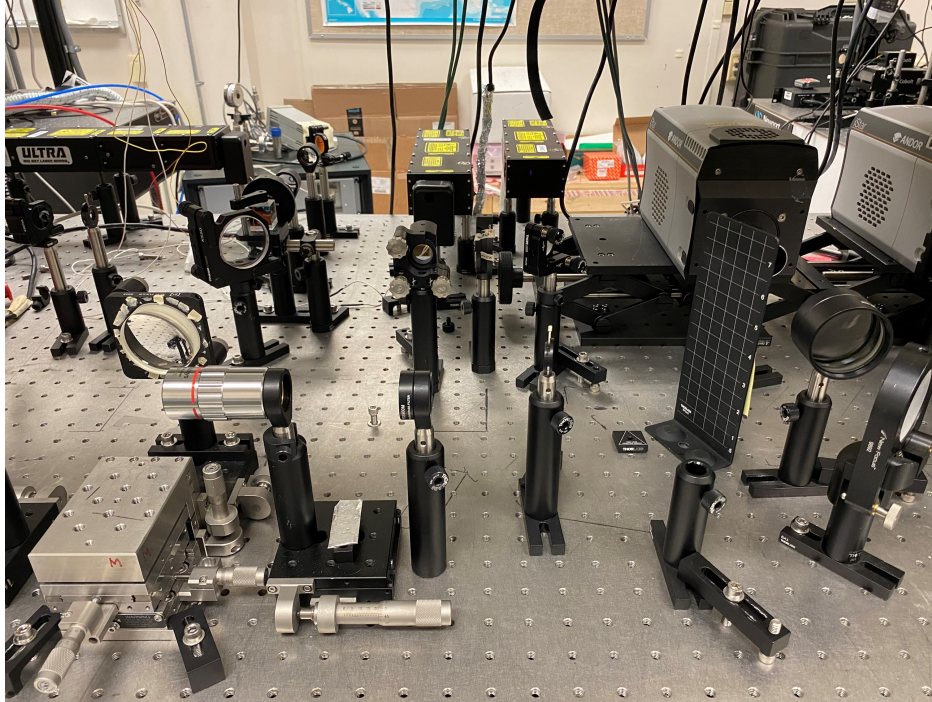


Figure 3.4: The laser ablation system used to ablate the physical entity. The Laser beam originates from the laser head in the center of the image. The beam then travels through two reflecting optics to reach the focusing optic and hits the surface which is mounted on the stage in the lower left corner of the image. To the right of the stage is a magnification lens and a band-pass filter which light generated by the plasma plume travels through before being imaged by the iCCD camera in the right of the image.

## 3.2 Virtual Representation

The virtual representation of the physical entity was created using COMSOL Desktop<sup>®</sup>, shown in Figure 3.5.

### 3.2.1 3D Modeling

The initial model of the physical entity was a 3 dimensional model defined in the COMSOL Multiphysics<sup>®</sup> user interface. The model combined three different multiphysics aspects: ray tracing of the laser light, the thermal change in the material due to the laser light, and the change in the surface geometry.

The model, which can be seen in Figure 3.6, contained an cylindrical piece of aluminum 6061 to represent the physical entity that would be ablated. This part was positioned with the center of the ablation region at the center of the disk. A beam splitter cube was added in front of the aluminum disk to reflect the simulated light rays to the disk and allow some of the light to travel to a simulated sensor.

The laser light in the simulation was defined using the ray tracing module in COMSOL Multiphysics<sup>®</sup>. The light originated from a point source at the coordinate system's origin. It then propagated forwards in

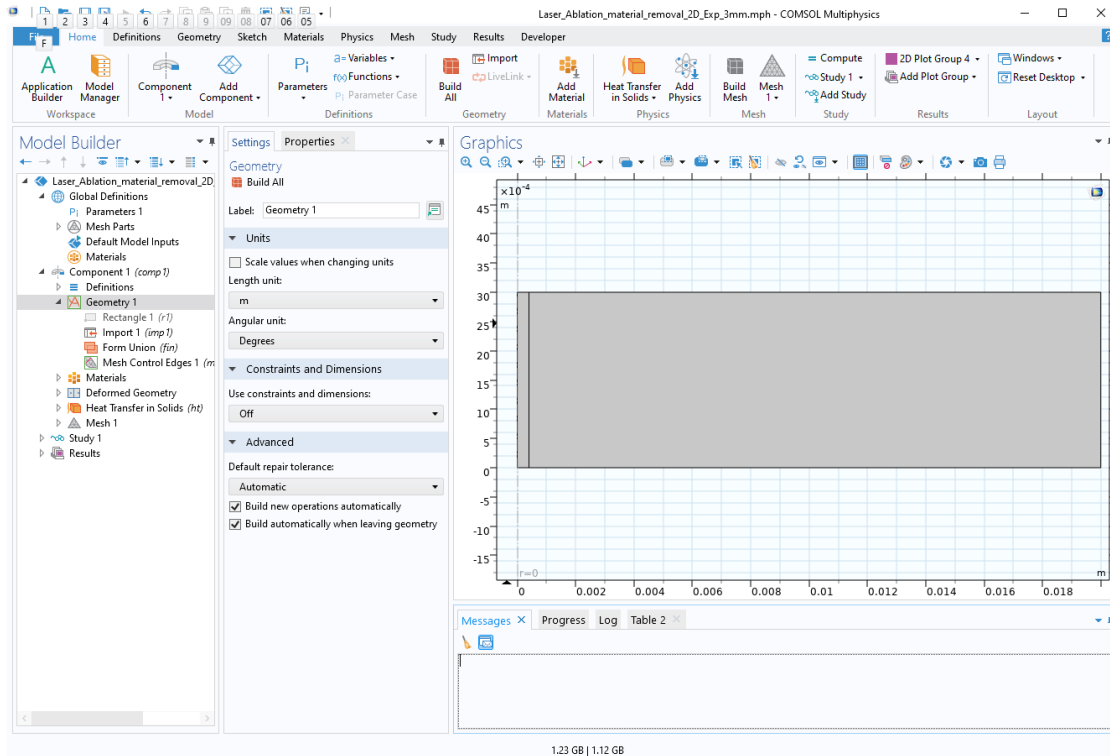


Figure 3.5: The COMSOL Multiphysics<sup>®</sup> user interface, also referred to as COMSOL Desktop<sup>®</sup>, which was used to create the virtual representation. The elements of the model are displayed in the left hand section. Parameter values of the model elements can viewed and edited in the center column and model elements can be viewed graphical in the right most section.

the x direction towards the beam splitter cube. When the light reached the cube, the beam split with 99 percent of the light reflected towards the target and the remaining one percent of the light passing straight through the cube to be collected on a simulated beam profile sensor. The output of the simulated sensor could be compared to the measured beam profile to confirm that the simulated beam matched the real beam. The light that traveled towards the target was absorbed by the surface upon impact. As the light hit the surface it was converted into thermal energy on the surface of the physical entity. This energy heated the material to high enough temperatures that the material was ejected into the surrounding air from the surface by evaporation. The resulting change to the surface in the three dimensional simulation is shown in Figure 3.7.

While this model provided a higher fidelity simulation of the ablation, it proved to be too computationally intense to be operated in real time. Initial simulations took upwards of 10 hours to complete half of the simulation when being performed on a Dell Latitude 7400 with an Intel Core i7-8665U processor. Reducing the mesh points in the aluminum disk did not alleviate the problem, due to the simulations failing to converge with a sparse mesh.



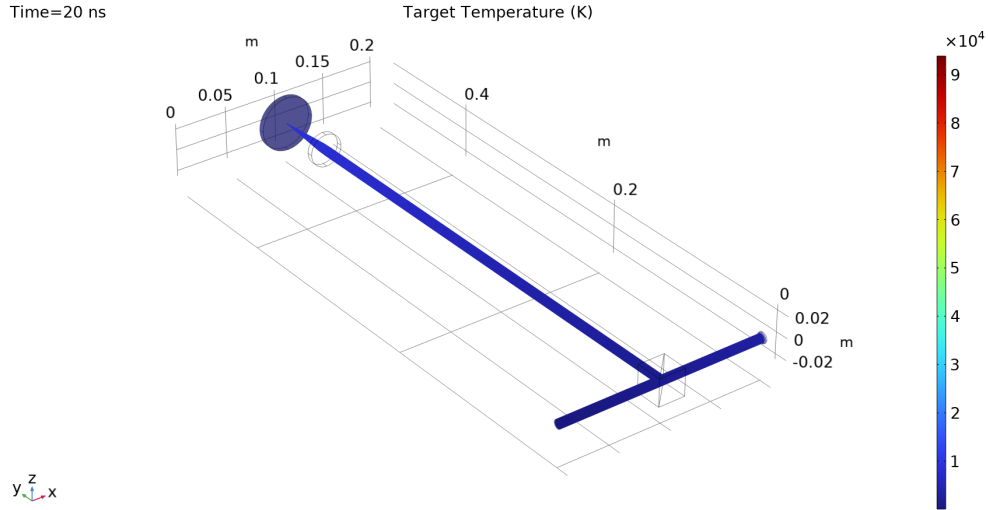


Figure 3.6: The three dimensional model displaying the heating of the aluminum target from the ray power being deposited on the surface. The beam begins at the bottom center of the image and travels to the right (along the positive x axis) towards the beam splitter cube, which is represented by the outline a cube. One percent of the light continues traveling to the right and is captured by the beam profile sensor, represented by a small disk. The remaining 99 percent of the light is reflected to travel upwards and to the left (along the y axis). The rays are focused by the lens, shown as an outline of a disk, onto the surface of the virtual representation of the aluminum alloy disk. The colorbar indicates the temperature scale of the target in degrees kelvin

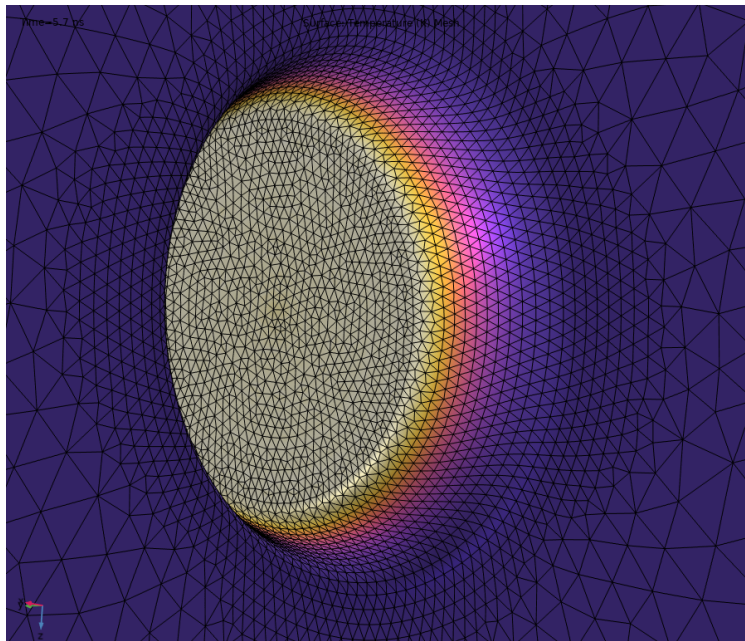


Figure 3.7: The indentation created in the surface’s mesh using the moving mesh module, viewed in the COMSOL Multiphysics® user interface. The color represents different temperatures of the material, with lighter colors indicating higher temperatures caused by heating from the laser beam.

### 3.2.2 2D Axi-Symmetric Modeling

Since the main objective of this project was to demonstrate the methodology of how a digital twin of a machined part can be created for use in industry, it was decided that creating a system that can function in a real-time capacity was more important than achieving a higher fidelity virtual representation. The computation effort of the simulation was reduced by changing the dimensionality from three dimensions to a two dimensional axi-symmetric simulation. Since the pulse was focused down to a spot only 0.3 mm in diameter, deviations in the beam's shape are combined together to create a smaller beam that is symmetrical about the central axis. Using this approximation the computational difficulty could be greatly reduced. The two dimensional model only required 2 to 10 minutes to complete the simulation using the same computer mentioned earlier, based on the amount of laser power used. With the transition to an axi-symmetric model, the ray tracing, beam splitter cube, and beam profiler sensor were removed, as they would not make physical sense in the new model. The energy from the laser pulse was then simulated using the Deposited Beam Power boundary condition in the Thermal Transfer in Solids module of COMSOL Multiphysics®. With the reduced time required for simulation the virtual representation could be used in real time between laser pulses during the laser drilling process.

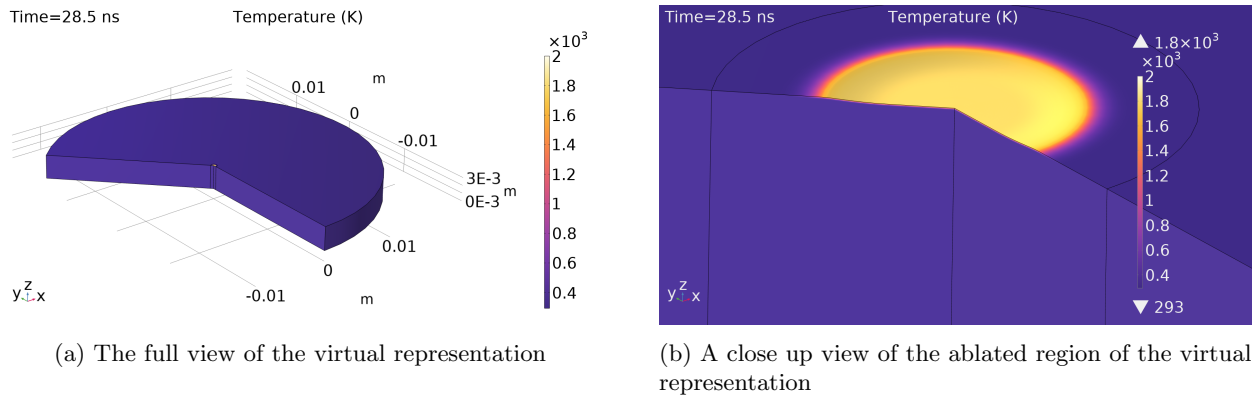


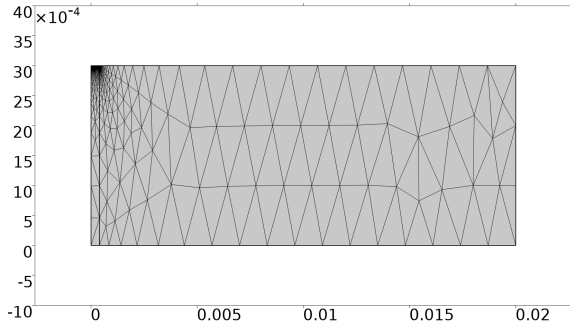
Figure 3.8: Views of the virtual representation in a 2D Axi-Symmetric model. The view is of the two dimensional description rotated about the central axis to express it in 3D dimensions. The colorbar on the right side of both images is the temperature in degrees kelvin

#### 3.2.2.1 Mesh Properties

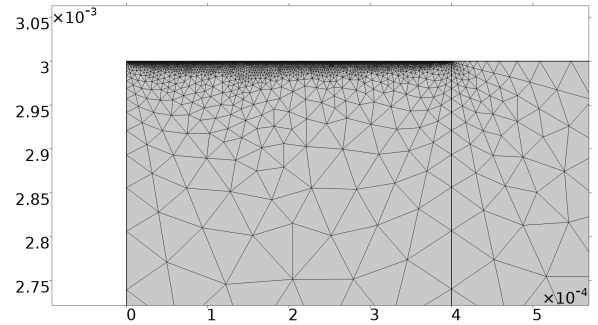
The quality of the simulation is dependent on the quality of the mesh used in the model. However as the number of mesh points increased, so did the computational effort required and the time needed per simulation. Due to the simulation's 2D nature, the mesh was generated as a set of triangular points in which each triangle is referred to as an element. To maintain a reasonable quality to the model and not waste computational effort on unneeded aspects of the model the mesh was designed with two different

Maximum Element Size	Simulated Ablation Depth	Simulation Time
10 $\mu\text{m}$	0.0608 $\mu\text{m}$	256 s
7.5 $\mu\text{m}$	0.1971 $\mu\text{m}$	212 s
5 $\mu\text{m}$	0.2947 $\mu\text{m}$	171 s
2.5 $\mu\text{m}$	0.3417 $\mu\text{m}$	208 s
1 $\mu\text{m}$	0.3668 $\mu\text{m}$	528 s
0.75 $\mu\text{m}$	0.3638 $\mu\text{m}$	1067 s
0.5 $\mu\text{m}$	0.3675 $\mu\text{m}$	2029 s
0.25 $\mu\text{m}$	0.3692 $\mu\text{m}$	4360 s
0.1 $\mu\text{m}$	0.3734 $\mu\text{m}$	20 725 s

Table 3.1: The reported ablation depth on the central axis and simulation time for an input energy of 15 mJ with varying maximum elements sizes for the mesh in the ablated region. The data was collected by performing the simulation with each of the maximum mesh element sizes listed and measuring the change in the mesh’s height along the central axis.



(a) The mesh points used in the laser ablation model.



(b) A zoomed in view of the mesh in region that is deformed by the laser ablation.

Figure 3.9: The mesh elements of the virtual representation are much smaller at the top of the disk close to the central axis. The elements are much larger as they move away from the point of impact of the laser, since the laser heating will only affect the small area at the top of the disk near the central axis.

specifications on the size of the triangle elements, as seen in Figure 3.9a. In the region closest to the central axis on the top surface, where the laser light impacts the surface and ablation is expected, the maximum element size of the mesh was 1  $\mu\text{m}$ . The relationship between the maximum element size, the simulation results, and the simulation time was explored in a mesh independence study, the results of which are in Table 3.1. 1  $\mu\text{m}$  was selected as the maximum element size because for values less than that, the results changed by up to 1.8% only and the time required for the simulation increased dramatically. For areas outside of the ablation region, the mesh was generated from the predefined normal spacing which had a maximum element size of 3.35 mm and a minimum element size of 15  $\mu\text{m}$ . The combination of the specifications created a mesh with a much denser set of elements on the top of the disk near the central axis. The mesh rapidly expands in the regions that do not require higher resolution, as shown in Figure 3.9b.

### 3.2.2.2 Thermal Transfer in solids

The input laser energy and thermal aspects of the simulation were handled by the Thermal Transfer in Solids module. Boundary conditions were used to instruct the simulation how to handle the interaction between the material, the laser pulse, and the environment.

#### Deposited Beam Power

To introduce the energy from the laser pulse into the simulation, the Deposited Beam Power boundary condition was used to provide the input thermal energy to the top surface of the material, as seen in Equation 3.1.

$$P_{deposited}(t, T) = \alpha(T) * P_{laser}(t) * rect(t) \quad [\text{W}] \quad (3.1)$$

$\alpha$  is the absorption coefficient which is a function of temperature,  $T$ ,  $P_{laser}(t)$  is the power of the laser at time  $t$ , and  $rect(t)$  is a simple rectangular function to ensure that the laser power deposited on the surface is zero outside of times when the laser pulse is impacting the surface. The absorption coefficient was added to the deposited energy to factor in the portion of the energy reflected back into the environment and that the reflection is temperature dependent [99]. The relationship between temperature and the absorption coefficient for an ideal 6061 Aluminum Alloy is presented in Equation 3.2 and Equation 3.3, which was derived by *Gao et al.* [99].

$$\alpha(t) = 0.365\sqrt{\rho(T)} - 0.0667\rho(T) + 0.003(\rho(T))^{\frac{3}{2}} \quad (3.2)$$

$$\rho(T) = \frac{\rho_{20}(1 + \gamma T)}{\lambda} \quad (3.3)$$

$\rho_{20}$  is the resistivity of the material at 20°C and  $\gamma$  is the temperature coefficient of resistivity. The power of the laser, Equation 3.4, is modeled as a Gaussian function with the center placed at  $t = 15$  ns and a full width at half maximum equal to 9 ns.

$$P_{laser}(t, E_{measured}) = \frac{E_{measured}}{3.8219 \cdot 10^{-9} \cdot \sqrt{2\pi}} e^{-\frac{1}{2} \left( \frac{t-15e-9}{3.8219e-09} \right)^2} \quad [\text{W}] \quad (3.4)$$

The rectangular function in Equation 3.1 is also centered at  $t = 15$  ns with a width of 22 ns for the non-zero region of the function. A transition zone of 0.1 ns on each side of the rectangle was added to make the

function continuous, which is seen Equation 3.5.

$$rect(t) = \begin{cases} 0, & t \leq 3.95 \text{ ns} \\ t \cdot 10^{10} - 39.5, & 95 \text{ ns} < t < 4.05 \text{ ns} \\ 1, & 4.05 \text{ ns} \leq t \leq 21.95 \text{ ns} \\ t \cdot -10^{10} + 220.5, & 21.95 \text{ ns} < t < 22.05 \text{ ns} \\ 0, & t \geq 22.05 \text{ ns} \end{cases} \quad (3.5)$$

### Ablative Heat Flux

As the material was being removed through evaporation, the thermal energy required for that transition from liquid to gas was removed from the material. This loss of energy, shown in Equation 3.6, was modeled as convective heat flux at the boundary of the material using Newton's law of cooling, with the temperature of the environment replaced with the boiling point of the material.

$$q_a = h_a(T - T_v) \quad [\text{W m}^{-2}] \quad (3.6)$$

$T_v$  is the boiling point of the aluminum alloy.  $h_a$  is the convection coefficient defined in Equation 3.7, which is zero for values of  $T$  less than zero and an arbitrary large slope for values greater than zero [100]. This causes the thermal energy to be removed quickly as the material is ablated.

$$h_a(T) = \begin{cases} 0, & T < 0 \\ T \cdot 10^9, & T \geq 0 \end{cases} \quad [\text{W m}^{-2} \text{ K}^{-1}] \quad (3.7)$$

In addition to the ablative heat flux, there is also heat loss due to black body radiation. The resulting heat flux is modeled with the Stefan-Boltzmann law, displayed in Equation 3.8.

$$q_r = \epsilon \sigma_{sb}(T^4 - T_{ext}^4) \quad [\text{W m}^{-2}] \quad (3.8)$$

### Other Boundary Conditions

The heat added by the Deposited Beam Power boundary condition dissipates within micrometers of the heated surface [101], resulting in the outer and lower edges being sufficiently far from the heated region that they were unaffected by the absorption of laser energy. Since these edges have no thermal flux they were

given the boundary condition of thermal insulation [102] that is seen in Equation 3.9.

$$-\vec{n} \cdot \vec{q} = 0 \tag{3.9}$$

The axi-symmetric nature of the model requires that the edge of the model on the central axis have a boundary condition of axial symmetry.

### 3.2.2.3 Deformed Geometry

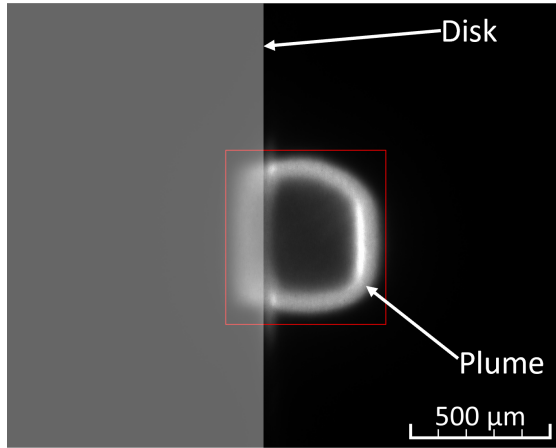
To simulate the removal of material as it was ejected from the surface, the Deformed Geometry module in COMSOL Multiphysics<sup>®</sup> was used. This module allowed the simulation to change the shape of mesh, thus making it possible to simulate the crater formation. The edge being deformed by the ablation was given the Prescribed Normal Mesh Velocity boundary condition. Only motion normal to the surface was considered, reducing both the computation effort required and the complexity of the modeling equations. This approach has minimal impacts to the accuracy of the simulation and is used in many nanosecond laser ablation models [103, 104, 88]. Additionally, any deformation as a result of the residual stresses from the thermal expansion and contraction was ignored. The velocity of the normal motion, presented in Equation 3.10, was derived from the heat flux due to the vaporization of the material [105].

$$v_a = \frac{q_a}{\rho H_v} \quad [\text{m s}^{-1}] \tag{3.10}$$

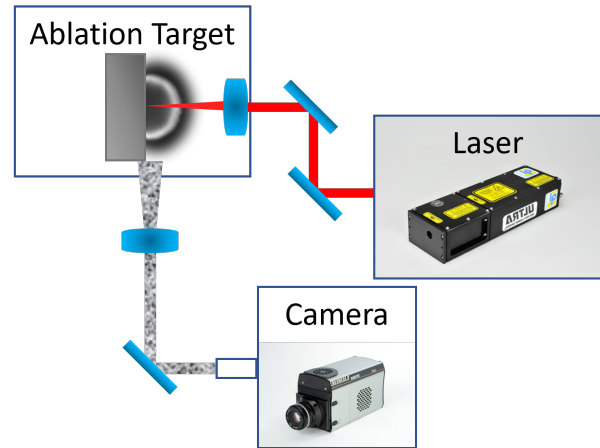
Where  $\rho$  is the density of the material and  $H_v$  is the heat of vaporization. The remaining edges of the disk did not have any motion due to the laser energy only heating the area of the impact. This was indicated to the model using another boundary condition within the Deformed Geometry module. The Prescribed Normal Mesh Displacement boundary condition was used with a fixed displacement of zero to forbid any motion of the outer edges.

## 3.3 Physical-to-Virtual Connection

To provide data to the virtual representation of the ablated part, an image of the plume generated during the laser ablation was captured. This image was collected using an iCCD camera with a shutter time in the nanoseconds range. The particular camera used was an Andor iStar DH334T-18U-73. The camera's shutter was opened 641.14  $\mu\text{s}$  after the laser energy was deposited on the surface of the material. This delay allowed the plume to expand and be recorded when it was at its largest.



(a) An image of the plume forming on the surface of the disk. The disk is not visible in the original image, so a semi-transparent layer has been added to illustrate the location of the disk.



(b) A diagram of the plumes are imaged. The system is viewed from above in the diagram.

Figure 3.10: The plume of evaporated material formed during the laser ablation of an aluminum target with the bounds of the plume in red. The vertical line protruding out of the top and bottom of the plume is the surface that is being ablated. The light to right of the vertical line formed by the protrusions is the plasma plume, while the light to left of the vertical line is the plume's reflection off of the disk's surface. The image is taken using the optics and camera seen in Figure 3.4.

The image of the plume was analyzed to determine the length between the left and right edges of the plume. In Figure 3.10, the plume can be seen rising off the surface of the disk. The disk is not visible due to the camera being configured to capture the high intensity of the light without over saturating. The vertical line that extends out of the top and bottom of the plume is the surface of the disk. The light to the right of this vertical line is the plume and the light to left of the line is the plume's reflection off of the physical entity's surface. To determine the width of the plume the image was first compressed into a one dimensional array composed of the maximum value in each column. The edges of the plume were then found by scanning through the array starting at both ends of the array and moving inwards. The process first identified the start of data by locating the first pixel on each side above the noise threshold. The edge was then selected by taking the innermost index of the longest continuous set of points with a positive derivative. The background values were reliably between 500 and 650, so a pixel value of 800 was chosen as the threshold for selecting data from the background. Once the left and right edges were found from the array of maximum column values, the index of the left edge was subtracted from the index of the right edge to get the width of the plume.

The width of the plume could then be used to determine the amount of energy deposited onto the surface of the material. The relationship between the plume width and energy deposited was not initially known, so empirical data was needed. To measure the energy contained in a single laser pulse, an energy meter was

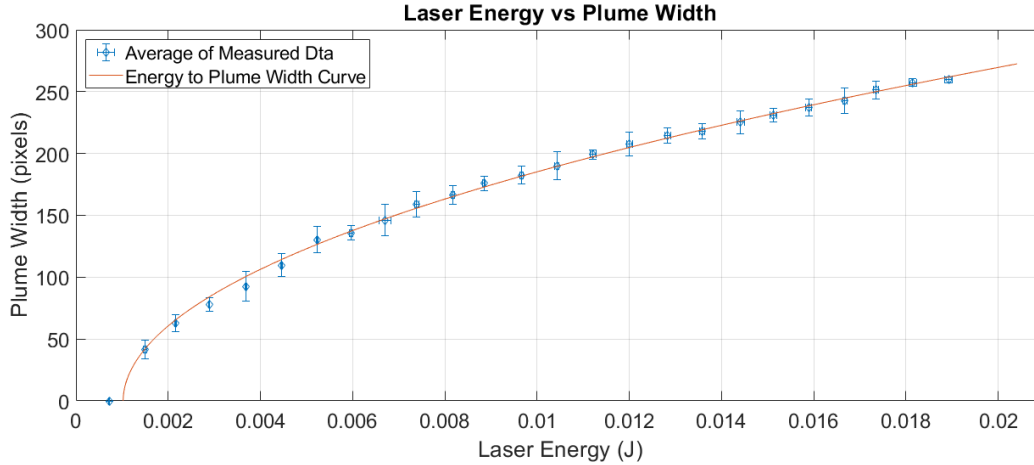


Figure 3.11: The averaged plume widths and energy readings at each different laser transmission level. A fit to the data is given in Equation 3.11.

used. The energy meter was mounted in the beampath of the laser, but further back than the stand that the ablated parts were set on during normal operations to avoid damaging the sensor. In this configuration either the plume or the energy could be recorded depending on if the target was present or not. To collect the energy measurements, the laser was fired with the transmission percentages set to integer values between 1% and 25%. The laser was fired ten times at the energy meter at each transmission value before progressing to the next transmission percentage. The full set of energy reading are listed in Table A.2 in the Appendix. To get a set of plume images to compare the energy readings to, the laser was fired another ten times while using the same transmission percentage values and the resulting plumes were recorded, seen in Table A.1 in the Appendix. The disk was not changed between the laser pulses since the previous ablations of the surface did not impact the size of the plume observed. The energy readings and plume widths for each transmission percentage value were averaged together to create a set of values that could be used to fit a curve to the data. Multiple curve fits were performed and the second degree polynomial seen in Equation 3.11 was found to best represent the data. The data used for fitting the curve can be found in the Appendix.

$$\text{Energy} = 2.60 \cdot 10^{-7} \cdot \text{Width}^2 + 3.98 \cdot 10^{-7} \cdot \text{Width} + 1.02 \cdot 10^{-3} \quad [\text{J}] \quad (3.11)$$

### 3.4 Virtual-to-Physical Connection

The virtual-to-physical connection provided two aspects to the digital twin: fault detection and determination of the energy still required to achieve the desired crater depth.



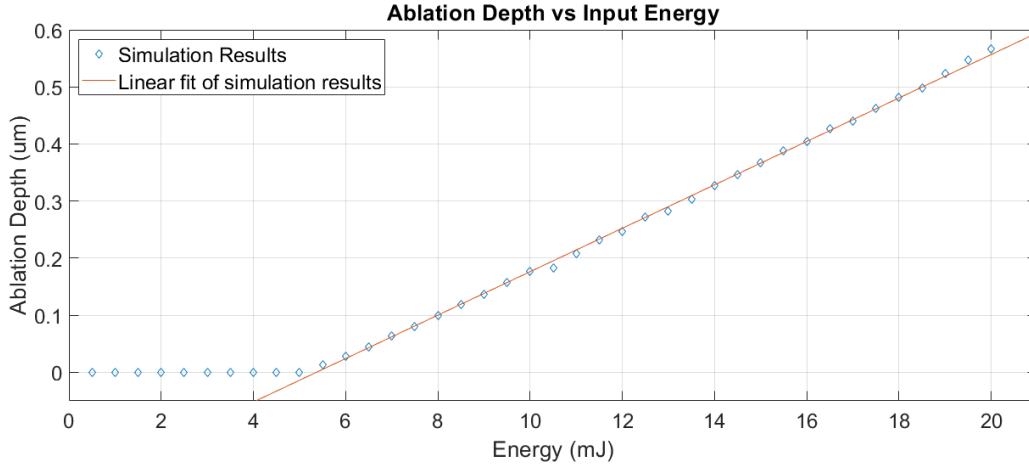


Figure 3.12: The relationship between the depth of the crater formed in simulation for a given energy value. The expression of the trend line is seen in Equation (3.12).

### 3.4.1 Process Control

The only means of controlling the amount of energy in each laser pulse was to adjust the amount of light passing through the attenuator mounted onto the front of the laser head. The transmission percentage necessary was determined though first calculating the remaining depth that needed to be ablated to achieve the desired depth. Next the required energy was found using the linear fit of the simulation data of the predicted ablation depth, Equation 3.12, for different energy levels, seen in Figure 3.12.

$$\text{Energy} = \frac{\text{Desired Depth} + 2.04 \cdot 10^{-7}}{3.80 \cdot 10^{-5}}, \text{ for Desired Depth} > 0 \text{ m} \quad [\text{J}] \quad (3.12)$$

Finally the transmission percentage needed was determined by using the linear relationship between the transmission percentage and the energy contained in the pulse, shown in Equation 3.13 and plotted in Figure 3.13.

$$\text{Transmission Percentage} = \text{Energy} \cdot 1314.34 + 0.17 \quad [\%] \quad (3.13)$$

That value would then be communicated to the attenuator before initiating another laser pulse. Due to the chaotic phenomenon that can happen in laser ablation, the transmission percentage had to be limited to 15 percent. Inspection of craters formed from laser pulses with higher transmission percentages above this threshold showed jagged raised sections in the ablation crater.

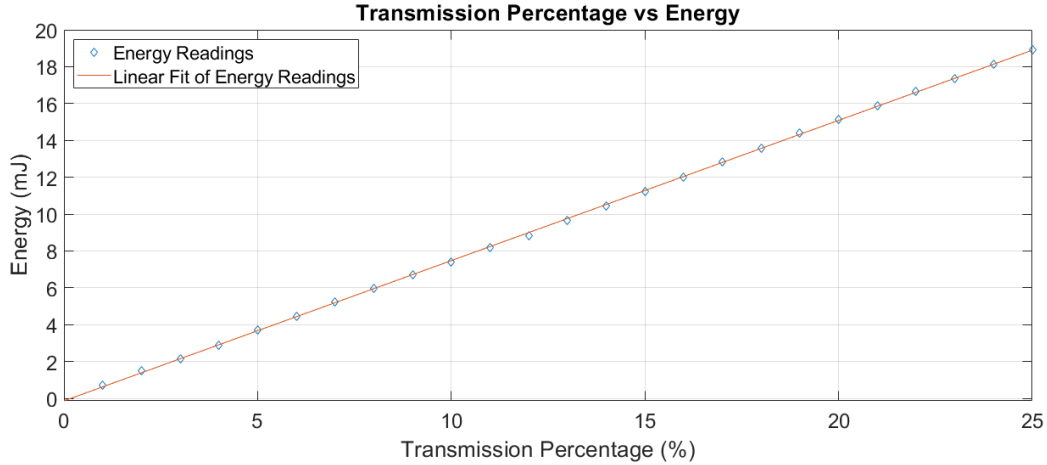


Figure 3.13: The relationship between the transmission percentage of the attenuator mounted on the laser and the energy with a pulse. The expression of the trend line is seen in Equation (3.13).

### 3.4.2 Fault Detection

To enhance the operation of the laser ablation system and alert operators when the ablated surface would not match the expected profile, a simple fault detection method was developed. The most observable feature of the laser ablation system was the plasma plume created by the ejection of material on the surface of the part. Using the images collected during ablation, deviations from the expected plume size can be observed and used as a basis for identifying fault conditions. Four different fault conditions were identified using the plume images and are discussed below.

#### 3.4.2.1 No pulse detected

In the event of insufficient energy to form a plasma plume, the image captured by the Andor iStar will consist of just background noise. This could be caused by a number of conditions, such as an obstruction in the beam path, the trigger signal not reaching the laser, or the Q-switch and flashlamp being in the wrong state. The lack of plume indicates that an insufficient amount of energy to cause ablation was deposited on the surface and that the material did not change. This fault condition would be detected by the maximum brightness value of all the pixels in the image being less than 700.

It is also possible that an issue with the timing of the camera could result in an image without a plume, despite the material being ablated. In this situation the fault detection routine would still alert the operator that no pulse had been detected. However, a characteristic pop as a result of the laser ablation would provide the system operator with evidence that the laser energy did reach the surface of the material. This combination of the audible sound of the ablation and the no pulse detected alert would indicate to the operator that the machining process should be stopped and the camera's timing be adjusted before restarting

the process. This condition is not expected after initial setup due to the time of the plume formation not changing.

#### **3.4.2.2 Pulse Energy lower than expected**

If a plume appeared smaller than expected that would indicate that the energy deposited on the surface was less than what was intended. This would still result in ablation as seen from the existence of a plume, but the amount of material removed would be lessened. An alert was designed to be triggered when the width of the plume is less than eighty percent of the expected value. This fault could be a result of a communication fault with the attenuator, dirty or damaged optics, or a fault in the flashlamp reducing the laser's output.

#### **3.4.2.3 Pulse Energy greater than expected**

On the other hand, if the plume is larger than expected that would indicate that the amount of energy deposited on the surface was larger than expected as well. This fault alert would be triggered by the width of the plume being greater than the expected value by five percent. The threshold for a larger than expected plume is only a difference of five percent, as opposed to the twenty percent for the other size threshold. This is a result of the change in plume size decreasing as the energy increased, which can be seen back in Figure 3.11. The larger energy delivered to the surface resulted in the profile of the ablation crater having jagged points rising out of the crater instead of the approximately flat surface predicted in simulations. There are two possible issues that could cause the energy to be greater than expected: a fault in the communication to the attenuation or a change in optics that reduced the losses in the beam path.

#### **3.4.2.4 Desired depth exceeded**

In addition to the possibly of jagged points in the ablation crater, pulses containing too much energy could cause an overshoot in the ablated depth. The fault detection routine would identify this by the measured depth of the virtual representation's crater at the central axis exceeding the desired depth by 0.1  $\mu\text{m}$ .

### **3.5 Digital Twin Application**

During initial prototyping, all of the tasks required for the digital twins to function were performed by hand. This included both controlling the equipment, which was done using their physical control panels, and computer based tasks, such as performing computations and running the laser ablation simulation. Several applications were used for the computer based tasks, which created a risk of transcription errors when performed by a human. There is also the risk of tasks being performed out of the required sequence,

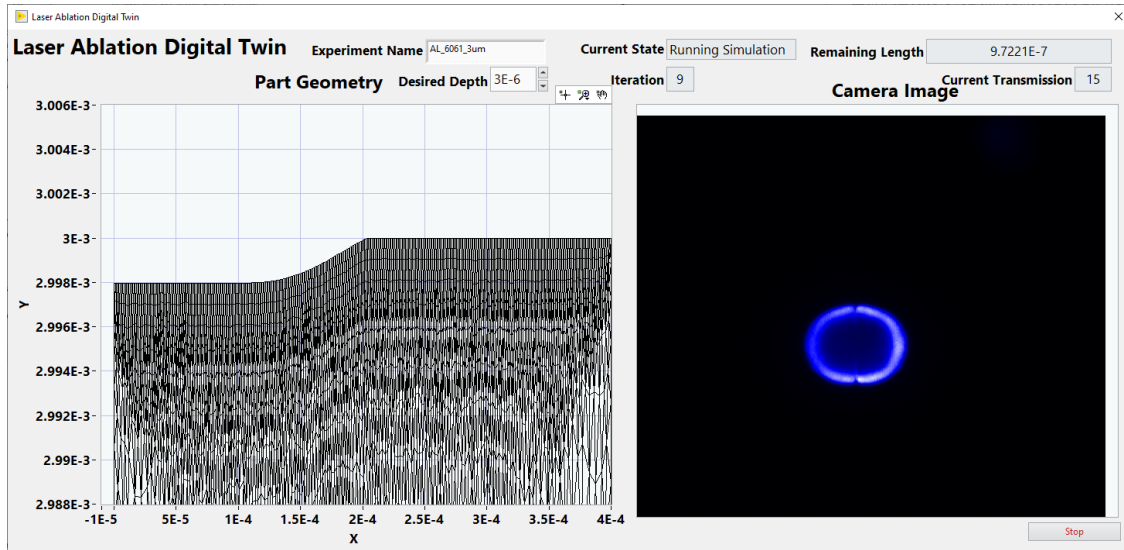


Figure 3.14: The application used to control the equipment, collect the plume images, and run the COMSOL Multiphysics<sup>®</sup> simulations. The graph in the left hand section of the interface displays the triangular elements of the mesh and the window in the right hand section shows the image of the plume captured from the most recent laser pulse.

which could have a dramatic impact on the synchronization between the physical entity and the virtual representation. For example, firing the laser twice instead of once or failing to change the transmission percentage would create a discrepancy between the two. For this reason, an application was created to handle the steps described previously in the methodology. The application was written in LabVIEW<sup>™</sup> due to it providing a simple way to create user interfaces and an existing familiarity with LabVIEW<sup>™</sup> programming. The user interface of the application created is shown in Figure 3.14. To perform the tasks required to control the laser ablation system and run simulations, routines were developed to interface with both the equipment used in the system and COMSOL Multiphysics<sup>®</sup>.

The LabVIEW<sup>™</sup> code, seen in Figure 3.15, has three main parts to it: starting the COMSOL Multiphysics<sup>®</sup> server and setting up the virtual representation; performing the laser ablations and simulations; and exporting the results and shutting down the COMSOL Multiphysics<sup>®</sup> server. The central part of the code, performing the laser ablations and simulations, is run in a loop which continues to execute until the desired depth has been met.

While COMSOL Multiphysics<sup>®</sup> does have an integrated development environment for creating models and simulating the physics acting on them, it was not suitable for use in this case. It could not operate in an autonomous fashion and would have introduced too many steps that would require data entry or initiation by a human operator into the laser ablation process. Fortunately COMSOL Multiphysics<sup>®</sup> can be used without the development environment by launching a server running COMSOL Multiphysics<sup>®</sup> and connecting to it.

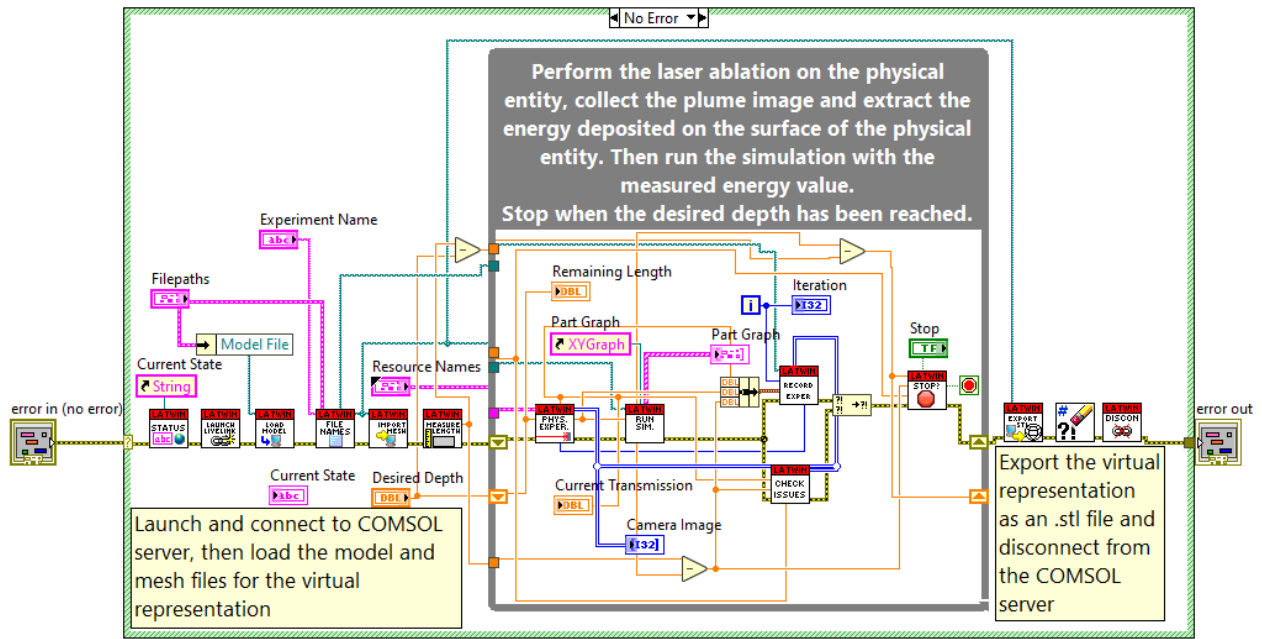


Figure 3.15: The block diagram of the LabVIEW™ code that controls the laser ablation system, extracts the energy measurement, and interfaces with COMSOL Multiphysics® to update the virtual representation.

Since there is no interface for direct communication between LabVIEW™ and COMSOL Multiphysics®, COMSOL's LiveLink™ for MATLAB® software was used to facilitate communication between the two environments. A set of LabVIEW™ functions were created as wrappers containing the MATLAB® code to perform the needed tasks to set up and use the COMSOL Multiphysics® model.

# Chapter 4

## Results

### 4.1 Initial Attempts

Early attempts at creating digital twins of the ablated disks showed that the application for controlling the laser ablation system and the COMSOL Multiphysics<sup>®</sup> model was able to successfully implement the control logic. However, there was a large discrepancy between the virtual representations and physical entities. This discrepancy was apparent in both the depth of the crater at the center and the shape of the crater. As can be seen in Figure 4.1, at the center of the crater jagged points reach up out of the crater. These features could be the result of multiple phenomena, such as explosive boiling or recoil pressure, that are too complex to be modeled in this application. Craters with similar topography to the one in Figure 4.1 consistently formed after being ablated with a laser pulse greater than 15 mJ. Repeated pulses were deposited onto the same

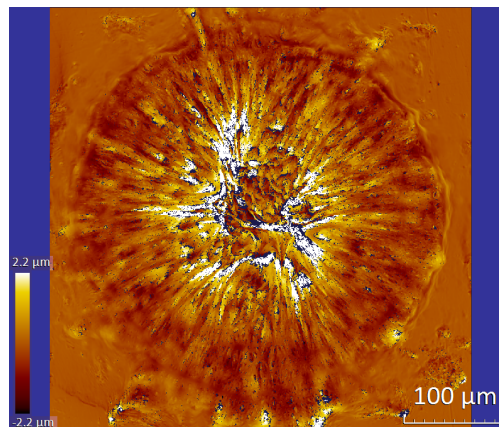
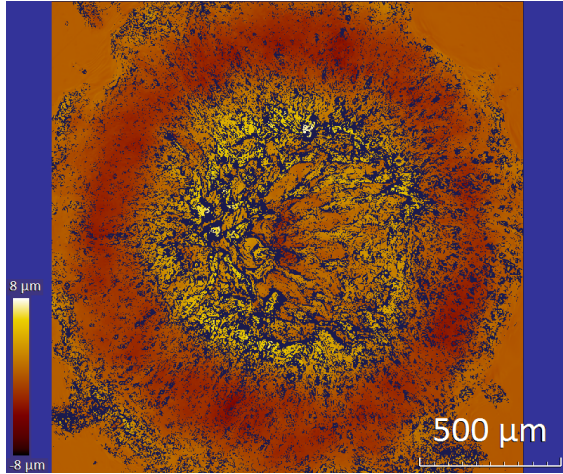
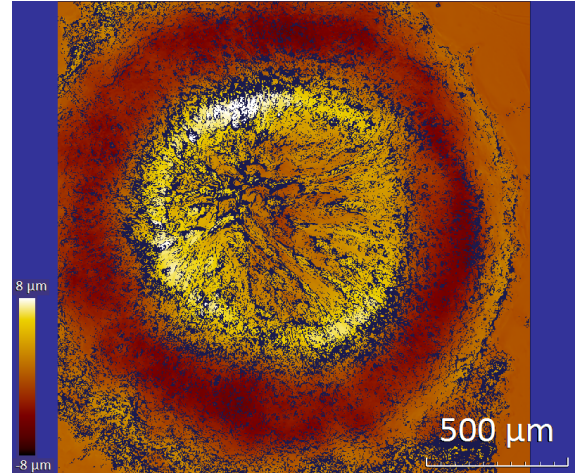


Figure 4.1: Depth profile of an ablation crater with jagged features rising upwards out of the crater. The colorbar in the lower left corner of the image indicates the depth, with positive values representing heights above the over flat surface. Darker colors indicate deeper locations of the crater.

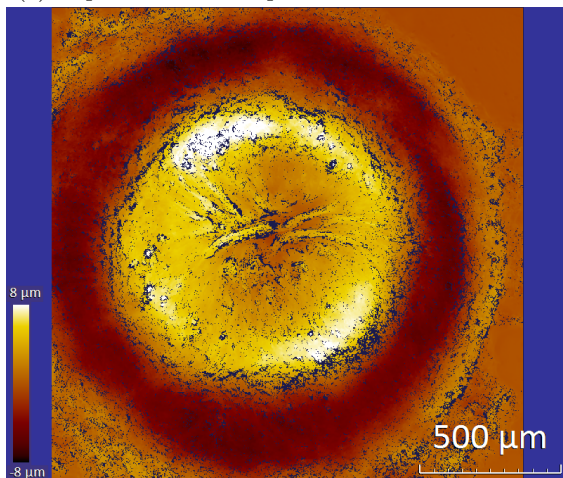
location on the surface to test whether the raised portions of the crater could be ablated away to form a smoother surface. This process only yielded partial success. The repeated laser pulse did remove the jagged points making the center smoother, but a raised mound was still left in the center of the crater with the outer ring continuing to get deeper, as evidenced in Figure 4.2.



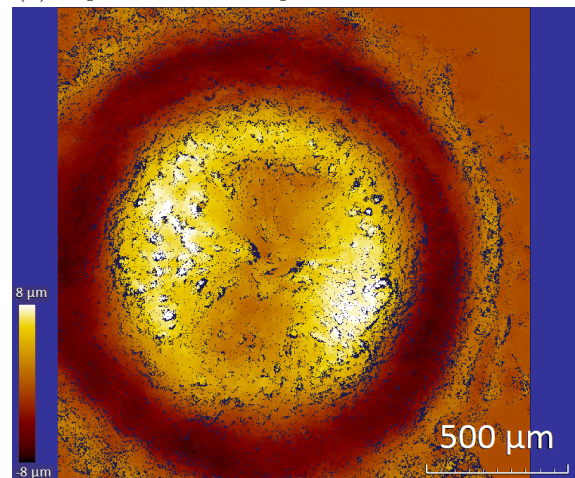
(a) Depth after 5 laser pulses at 30% transmission



(b) Depth after 10 laser pulses at 30% transmission



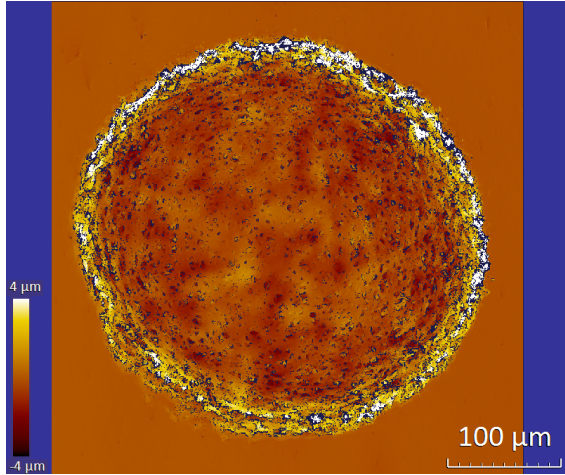
(c) Depth after 15 laser pulses at 30% transmission



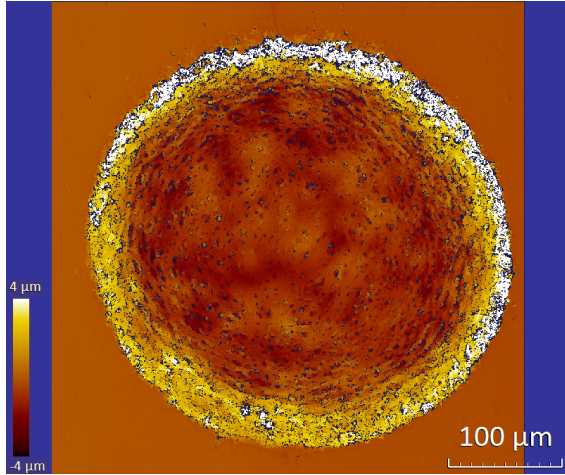
(d) Depth after 20 laser pulses at 30% transmission

Figure 4.2: The crater depth after multiple laser pulses have impacted the surface of the material with the attenuator set to thirty percent transmission. This amount of energy created a jagged surface with points reaching up out of the crater and would not match virtual representations. The jagged points were smoothed out after repeated pulses, however a raised mound remained in the center of the crater, as seen in the lower right image.

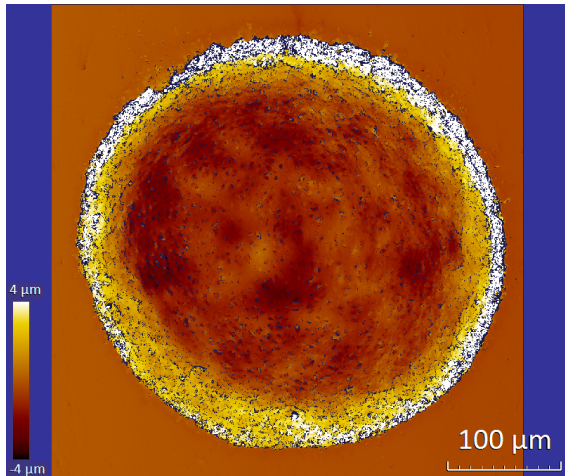
More accurate simulations of laser ablation exist [84] than the simple model developed in COMSOL Multiphysics<sup>®</sup> for this application, however utilizing them would have increased the time required for each simulation and would still not account for all of the physics occurring in reality in the way that a first principles model could. In the initial attempts using a three dimensional model, which still did not account for all of the physics involved, the simulations required over ten hours for a single pulse. Using this would have



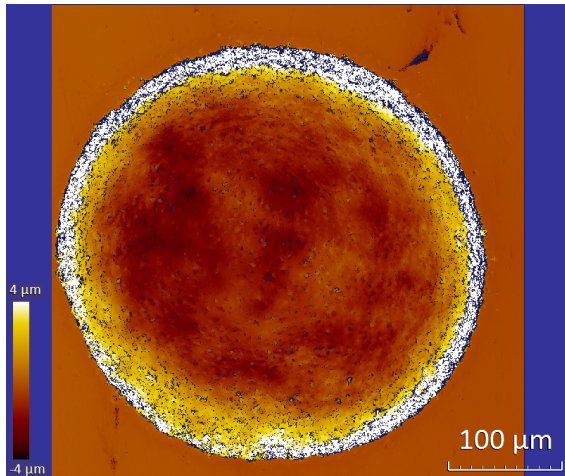
(a) Depth after 5 laser pulses at 10% transmission



(b) Depth after 10 laser pulses at 10% transmission



(c) Depth after 15 laser pulses at 10% transmission



(d) Depth after 20 laser pulses at 10% transmission

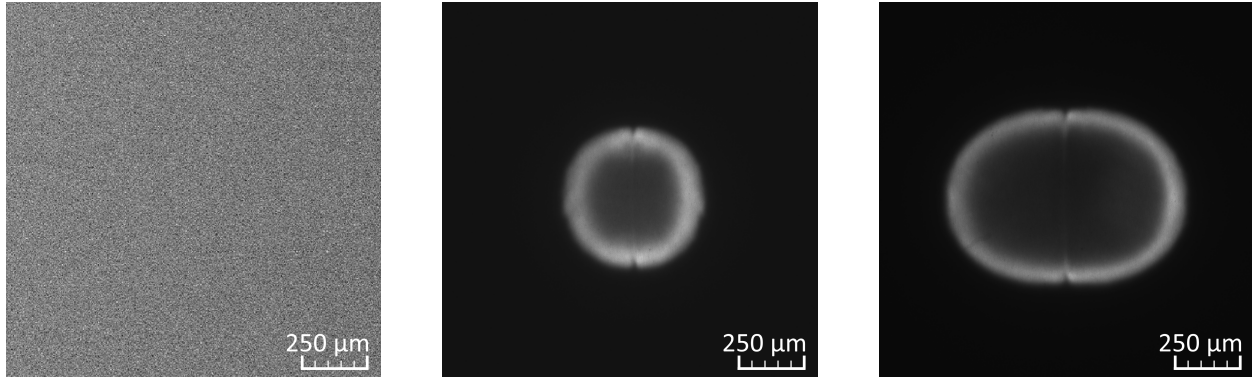
Figure 4.3: The crater depth after multiple laser pulses have impacted the surface of the material with the attenuator set to ten percent transmission. With lower energy levels the craters were much smoother and more closely resembled the craters formed on the virtual representations.

made the twinning rate untenable for real-time operation. For this reason a two dimensional axisymmetric model was used and the laser energy was confined to a region where the simpler model is accurate enough for this project. Fortunately when the laser energy is kept below 15 mJ, the produced surface is much smoother and more closely reflects the output of the simulations, shown in Figure 4.3.

## 4.2 Fault Detection

Monitoring the images of the plumes used to determine the amount of energy deposited on the surface of the physical entity, allowed for the fault detection to be conducted. The fault detection methodology was tested to ensure it was able to catch when a fault occurred.





(a) The background light when no plume observed.

(b) A small plume generated when the laser energy is lower than expected.

(c) A large plume generated from too much energy in the laser pulse.

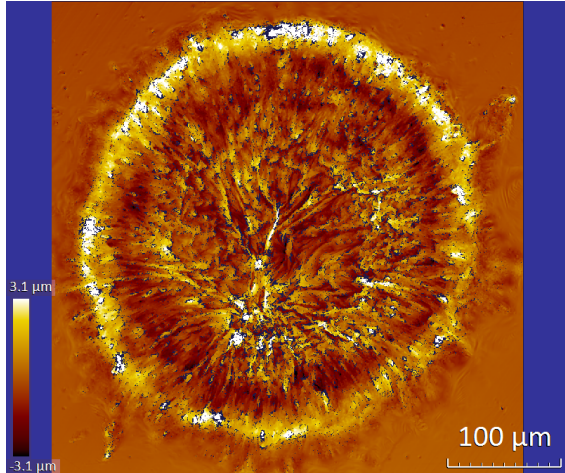
Figure 4.4: Camera images displaying the three fault conditions that can be determined using the plume imaging. The images display the side of the plume and the plume’s reflection in the surface of the disks. They were captured at the same horizontal position as the plume, from the plume’s right side.

#### 4.2.1 No Plume Detected

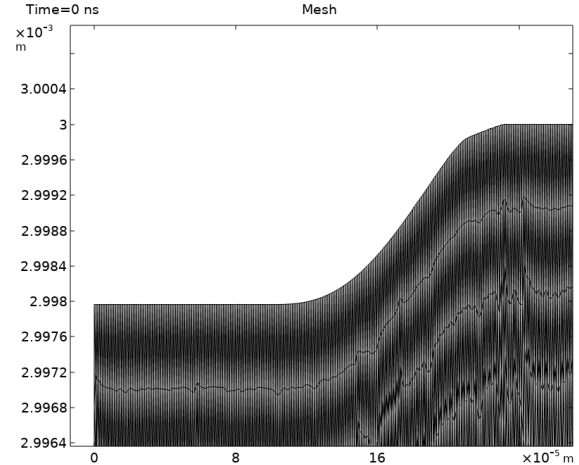
To confirm that the lack of a plume could be detected, the manual shutter on the laser was closed before the laser fired. The fault was successfully detected by applying the threshold approach described in section 3.4.2. The fault occurring did not adversely affect the difference between the virtual representation and the physical entity. Since no energy reached the surface, it was not ablated and the geometry was not the changed. The lack of a plume in the image was also interpreted by the physical to virtual connection as zero energy, which would result in zero change to the virtual representation during the simulation. The application alerted the user to the fault and continued operating afterwards.

#### 4.2.2 Low Energy

When the energy contained in a pulse went below the normal range of the variation, the image processing routine in the physical to virtual connection was able to detect the deviation. This was tested by inserting a routine into the LabVIEW<sup>TM</sup> application that lowered the transmission percentage after it was determined for the next laser pulse. When tested, the low energy fault was successfully detected by the fault detection routine. The low energy value was inputted into the simulation resulting in less change to the crater on the virtual representation. Since the virtual representation provided an expected depth of the crater, the fault was automatically mitigated by the routine in the virtual to physical connection that computes the transmission percentage required.



(a) The crater on the physical entity after receiving a pulse with too much energy



(b) The virtual representation of the surface, which is smooth unlike the physical entity.

Figure 4.5: Laser pulse with too much energy creates a vastly different and unpredictable surface that the virtual representation can not match.

### 4.2.3 High Energy

The detection of a high energy fault was tested in the same fashion as the low energy fault, by adding a routine to the LabVIEW<sup>TM</sup> application that increased the transmission percentage before being communicated to the attenuator. The fault detection routine was successful in identifying this fault and alerting the user to its occurrence, as displayed in Figure 4.6. The effect of the laser energy being greater than expected is more likely to have an adverse effect on the difference between the physical entity and the virtual representation than the other fault conditions. As already shown in Figure 4.1, a high energy pulse can cause the surface to be extremely rough and create jagged points that rise up out of the crater. This deformation caused deviation between the virtual representation and the physical entity that could not be corrected. This difference can be seen in Figure 4.5. Once the fault had occurred the crater could be smoothed out to a certain degree, similar to the change in the craters in Figure 4.2. However unless there was a large distance to the desired depth, the repeated pulses needed would remove too much material from the physical entity and overshoot the desired crater depth.

### 4.2.4 Depth Exceeded

The final fault condition was observed when the depth of the virtual representation's crater was greater than the desired depth. This was also tested by increasing the transmission percentage used to deliver a larger pulse and ablate more material from the surface. Due to the virtual to physical connection monitoring the depth and determining the transmission percentage of the laser light, this condition was only witnessed in

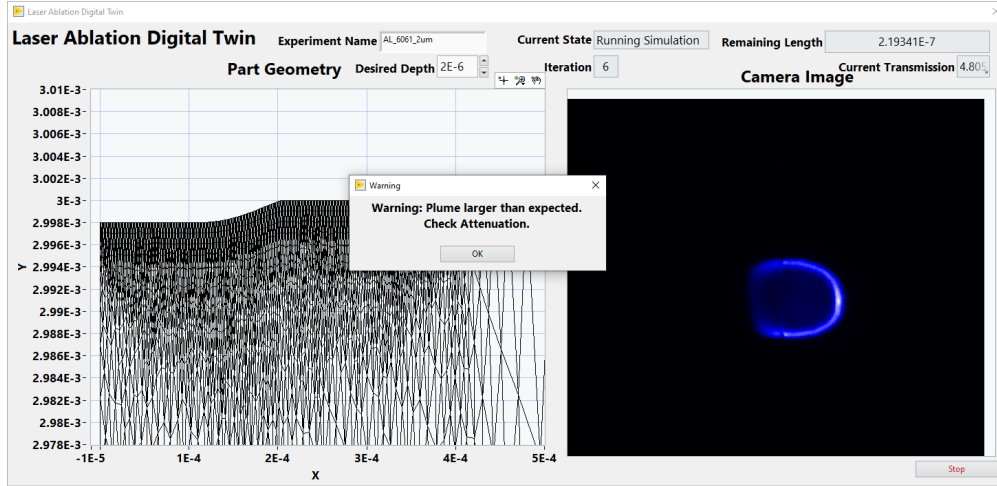


Figure 4.6: The application dashboard alerting the user to the laser pulse containing more energy than expected.

combination with the high energy fault. This fault condition was also successfully detected by the fault detection routine.

### 4.3 Physical Entity to Virtual Representation

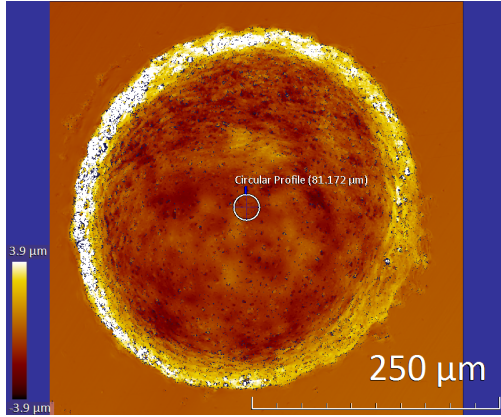
Once the control logic determining the transmission percentage in each pulse had been modified to use a maximum of 15%, the shape of the craters formed on the virtual representations were more characteristic of the craters on the physical entities. To compare the depth of the crater on the physical entity and the crater on the virtual representations, digital twins were created with intended crater depths of 1  $\mu\text{m}$ , 2  $\mu\text{m}$ , and 3  $\mu\text{m}$ . The measurement of the craters formed on the physical entity was performed using an optical profiler. The particular optical profiler used was a Zygo ZeGage<sup>TM</sup> fitted with a 20x magnification objective. The measurements taken with the Zygo ZeGage<sup>TM</sup> have a surface topography repeatability of  $\leq 3.5$  nm, which can be used as estimate of the uncertainty of the measurement. Twelve different attempts at creating digital twins were performed to fine tune the synchronized operation of the laser ablation system, the COMSOL Multiphysics<sup>®</sup> simulation, and the LabVIEW<sup>TM</sup> application. When the system began operating smoothly, a new set of calibration data was collected, found in Tables A.1 and A.2 in the Appendix, and the three digital twin test cases discussed below were created. The three test cases were created to test how much the virtual representations deviated from the physical entities. Three different ablation depths were used to see how varying the amount of material removed affected the deviation. The results of the three test cases are in Table 4.1.

The crater formed in the 1  $\mu\text{m}$  ablation experiment, seen in Figure 4.7, has a rough surface that does not

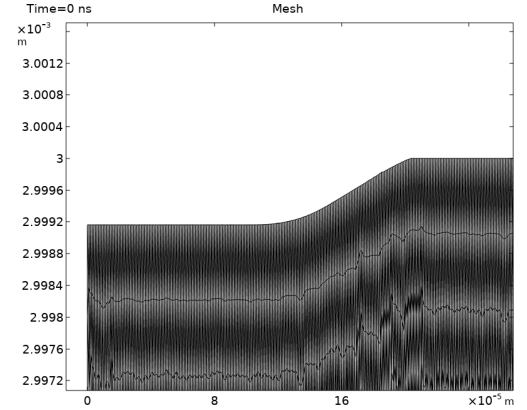
Intended Depth	Depth of physical Crater	Depth of Virtual Crater	Difference	Error
1 $\mu\text{m}$	1.012 $\mu\text{m}$	0.837 $\mu\text{m}$	0.175 $\mu\text{m}$	20.8%
2 $\mu\text{m}$	1.431 $\mu\text{m}$	2.001 $\mu\text{m}$	0.570 $\mu\text{m}$	28.5%
3 $\mu\text{m}$	2.012 $\mu\text{m}$	3.073 $\mu\text{m}$	1.061 $\mu\text{m}$	34.5%

Table 4.1: Comparison of the depths of the craters on the physical entities and the virtual representations.

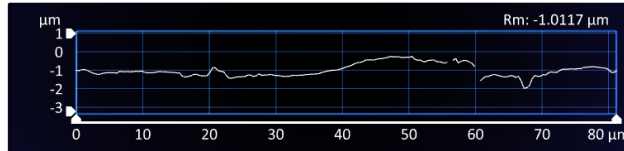
match the smoothness of the surface in the virtual representation. The average depth of physical entity’s crater was 1.012  $\mu\text{m}$  over a circular profile at the center of the crater, shown in Figure 4.7c. The depth of the crater formed in the virtual representation was 0.837  $\mu\text{m}$ , representing a 20.8% difference.



(a) The crater in the center of the physical entity.



(b) The digital twin’s surface after the simulated ablation. The simulated crater depth is 0.837  $\mu\text{m}$ .

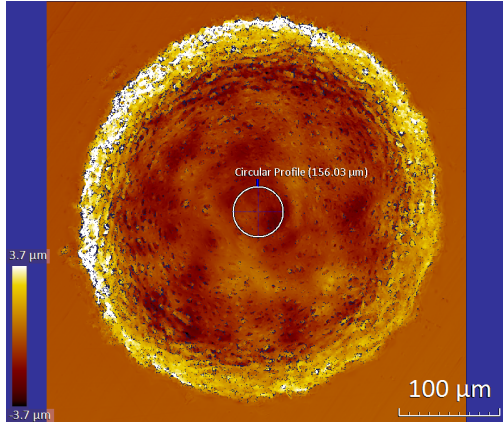


(c) The depth profile over the circle in (a).

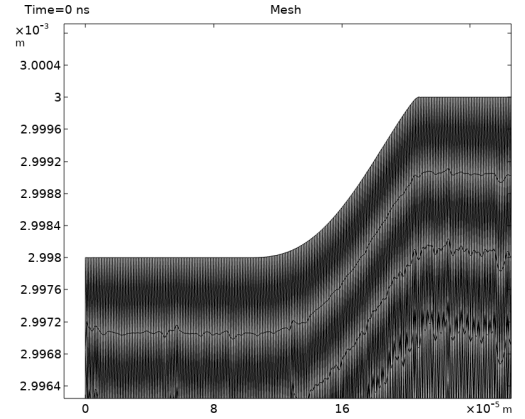
Figure 4.7: The virtual representation of the surface and the optical profiler measurements of the physical surface for the 1  $\mu\text{m}$  test case. The average depth over the circle in (a) was 1.012  $\mu\text{m}$ .

When attempting to drill a 2  $\mu\text{m}$  deep crater, the difference between the depths of the craters on the physical entity and the virtual representation grew. The crater created on the physical entity had an average depth of 1.431  $\mu\text{m}$  over the circular profile displayed in Figure 4.8c. The virtual representation had a crater depth of 2.001  $\mu\text{m}$ . This created a difference of 28.5% between the two craters.

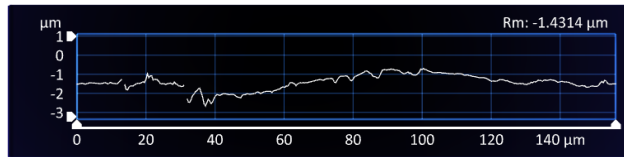
The results from the attempt to make a 3  $\mu\text{m}$  deep crater show a physical entity with a smoother surface. The smoother surface holds a closer resemblance to the smooth surface of the virtual representation than the results from the 1  $\mu\text{m}$  and 2  $\mu\text{m}$  experiments. However the numerical difference in crater depth is larger than in other the demonstrations. The physical entity had a crater with an average depth of 2.012  $\mu\text{m}$ , while the virtual representation’s crater was 3.073  $\mu\text{m}$  deep. The difference between the two craters was 34.5%.



(a) The crater in the center of the physical entity.

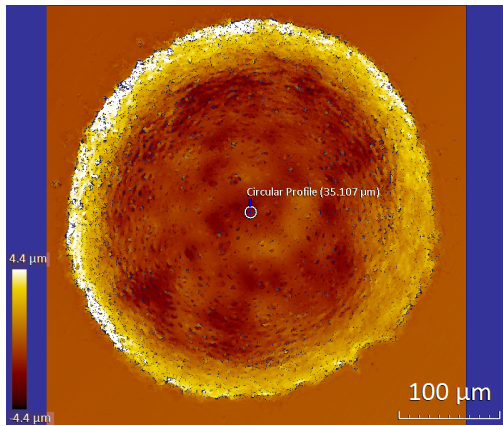


(b) The digital twin's surface after the simulated ablation. The simulated crater depth is 2.001  $\mu\text{m}$ .

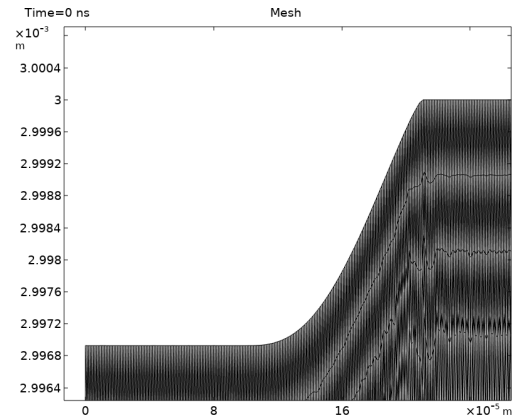


(c) The depth profile over the circle in (a).

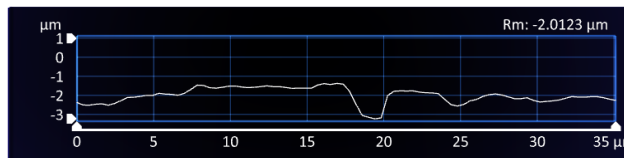
Figure 4.8: The virtual representation of the surface and the optical profiler measurements of the physical surface for the 2  $\mu\text{m}$  test case. The average depth over the circle in (a) was 1.431  $\mu\text{m}$ .



(a) The crater in the center of the physical entity.



(b) The digital twin's surface after the simulated ablation. The simulated crater depth is 3.073  $\mu\text{m}$ .



(c) The depth profile over the circle in (a).

Figure 4.9: The virtual representation of the surface and the optical profiler measurements of the physical surface for the 3  $\mu\text{m}$  test case. The average depth over the circle in (a) was 2.012  $\mu\text{m}$ .

## 4.4 Discussion: Crater Depth Differences

The craters formed on the physical entity and the virtual representation, displayed earlier in the chapter, have differences of up to 34.5% in their depths. The deviation between the physical and virtual craters is primarily caused by the simulation only capturing a portion of the physics occurring during the process. The deviations increased as the number of laser pulses used increased. As noted before, more aspects of the physics could have been modeled, such as fluid flow or the thin layer of oxide on the material [88]. However, this would have increased the time required to compute the change to the virtual representation further diminishing the ability for the system to operate in real time. It also would not have been feasible to perform multiple pulses and simulate the collective change to the surface with a single simulation. Since the surface cools between each pulse the simulation needs to compute the effects of each pulse individually. Furthermore, this would interfere with the process control aspect of the digital twin, since the input energy of the next pulse is determined from the crater depth in the virtual representation. The additional time required by a more sophisticated model would have made the digital twin not feasible for industrial usage without further investment in computational resources and data collection. However, if those resources are available there are at least two approaches to developing a better simulation; a first principles model or a neural network.

Utilizing a first principles simulation of laser ablation would be possible [92, 91]. However this would have a dramatic impact on the time required to simulate the effects of the laser pulse. Given the large computational expense of just running the simulation in three dimensions, computing a complete model of the physical process would be too large. This is demonstrated in the effort by Sonntag *et al.* [93] to simulate the molecular dynamics, which required 500,000 CPU hours to simulate the 254.5 ps of a femtosecond laser ablation. While the computational power accessible has increased since then, high fidelity simulations are still performed on large computing clusters [84]. Even with the computation resources to perform a first principles simulation, the simulation time would be too great for a real-time usage of the resulting surface profile.

Instead of attempting to create a higher resolution model, a deep neural network could be used to model the changes to the surface [94]. With a trained model, the surface and laser pulse parameters could be inputted into a model which could more efficiently predict the resulting surface of the physical entity. The trade off for the increased efficiency of a neural network is the effort required to collect the data used for training. This would add a large investment in time and equipment to build datasets. Tani *et al.* [94] used between 3,700 and 39,000 datasets of laser ablation experiments to train models on different materials. Both the time and equipment needed to train a neural network placed this method outside the scope of this

project, however it is worth noting that using a neural network would provide high resolution changes to the virtual representation and maintain the real-time digital twin synchronization.

## Chapter 5

# Conclusion

In order for digital twins to be useful in the manufacturing industry, a large volume of examples must exist for system designers that are feasible in industrial settings. The methodology presented above demonstrated the creation of digital twins of laser drilled parts and was used to create three proof-of-concept test cases using currently available tools. These digital twins serve as an example of how digital twins can be developed for precision machined products. Manufacturing facilities could leverage them to monitor the progress of an operation, detect issues occurring during the process, provide inputs to the control logic, and deliver models of individual machined parts to customers. Currently the existing literature on digital twins lacks sufficient examples to enable adoption of digital twins by manufacturers. This research contributes to the expanding body of work on digital twins and will hopefully provide an example for system designers of how the concept can be leveraged for laser drilling. Future researchers will be able to expand on the methodology presented here by incorporating more efficient and higher fidelity models. While the virtual representations and physical entities had large discrepancies; with improved models and computational resources the methods employed would deliver digital twins that could be utilized in laser drilling applications.

To demonstrate how a digital twin could be used in machining, crater formation during laser drilling was selected as an application. To facilitate the laser drilling a pulsed laser ablation system was used. The digital twins consisted of virtual representations of 6061 Aluminum alloy disks. These virtual representations existed as geometric descriptions of the 6061 aluminum disks created in COMSOL Multiphysics<sup>®</sup>. The geometric descriptions were kept up to date with the physical entities by simulating the changes caused by laser ablation using the input energy. The energy reading was provided by the physical-to-virtual connection, which used an iCCD camera and an image processing routine. The camera captured images of the plumes generated on the surfaces of the physical entities and the image processing routine extracted the widths of the plumes in



the images. Those widths were converted to energy values using a relationship found from empirical data. The virtual-to-physical connection could then provide the process control and fault detection to the system. By taking measurements of the depths of the craters on the virtual representations the predicted remaining ablation depth was found. Using that remaining depth and a relationship between the incident energy and the predicted ablation depth, the energy required for the next pulse was calculated. The needed energy for the pulse was converted to the transmission percentage, using another relationship found from empirical data, and communicated to the attenuator. The pulse would then be fired and the process would repeat until the desired ablation depth was reached in the virtual representation. In addition to the process control, a fault detection routine would check for issues as the surface of the physical entities were being ablated. The routine monitored for four different fault conditions: no plume being generated, lower than expected energy, higher than expected energy, and the ablated depth exceeding the desired depth. Each fault condition was created purposefully to test that it could be detected by the fault detection routine. In all four cases the fault detection was successful in detecting and alerting the user to the fault.

To further illustrate that this methodology was not just a framework of what could be done, three digital twins were created as test cases. By creating the digital twins it demonstrates that the methodology is more than simply an idea of how a digital twin could function. The necessity of the digital twin actually functioning, required that each of component of the system be created with real world considerations of what resources and tools might be used in an industrial setting. Three different ablation depths were used to test the performance of the digital twin over different crater sizes. The 1  $\mu\text{m}$  case showed good agreement between the depths of the physical entity's and the virtual representation's crater. However the surface of the physical crater differed from the virtual representation's crater in terms of the roughness of the surface. The digital twin's simulations produced a crater that was much smoother than the physical entity due to the assumed rotational symmetry and the simplified aspects of the simulation. When the desired depth was increased to 2  $\mu\text{m}$  the difference between the depths of the physical crater and virtual crater increased to 28.5% and the surface of the physical entity became smoother. This trend continued with the 3  $\mu\text{m}$  depth test case, the difference increased to 34.5% and the surface was the smoothest of the three test cases. The increase in smoothness can be attributed to the repeated pulses having a smoothing effect on the surface. The correlation between the crater smoothness and the number of laser pulses used can be seen in the test data of repeated pulses and the three test cases. The change in accuracy is more difficult to explain and could be the result of higher level physics not captured in the simulation environment. As noted in the methodology, the exclusion of these higher order phenomena was an intentional choice to keep the simulation runtime short enough to be useful in real time. Even with the accuracy decreasing as ablation depth increased, the project fulfilled its main objective of demonstrating how a digital twin could be created and used during a

machining process. Those in the manufacturing industry could replicate the methodology and modify it to fit their own applications. The feedback loop generated would allow for automated routines to monitor and control the laser drilling of materials.

Further improvements to the quality of the virtual representation could be made to both improve the speed and accuracy of the simulation. The most likely approach to yield success would be using a neural network instead of a multiphysics simulation. While it would require a lot of upfront effort to gather the necessary training data for each material being ablated, it could be worthwhile in industrial applications. The work of Tani *et al.* [94] showed promise in how a neural network could be used to deliver fast and accurate predictions of the crater profile. By exchanging the multiphysics simulation with a neural network, this methodology could be expanded to be used in industrial ultra-precision machining factories.

The usage of digital twins, similar to ones described earlier, could enable the manufacturing industries to leverage the volumes of data that are now accessible. By feeding real world sensor data into digital twins of the objects progressing through their production facilities, manufacturers can monitor the virtual representations. This would allow them to potentially increase the precision and efficiency of their operations through better process control and fault detection. Future advances in computing and automation will enable the usage of high fidelity models that are able to operate in real time, and will empower manufacturers to incorporate digital twins as we progress through the fourth industrial revolution.

## Acknowledgment

This work was performed under the auspices of the U.S. Department of Energy by Lawrence Livermore National Laboratory under Contract DE-AC52-07NA27344.

# Appendix

Transmission (%)	Plume Width (Pixels)
1	0,0,0,0,0,0,0,0,0
2	44,39,35,43,40,43,46,37,43,46
3	63,60,63,61,63,66,59,59,69,67
4	83,76,76,77,73,79,79,79,80,79
5	86,90,87,89,98,89,95,106,95,91
6	106,112,114,103,112,115,103,112,114,107
7	131,132,121,135,130,137,137,125,128,127
8	138,134,140,134,140,135,135,135,131,137
9	139,148,141,155,149,152,144,153,141,137
10	153,161,165,159,156,154,168,152,161,158
11	169,167,166,163,162,166,163,175,164,168
12	176,173,179,177,174,174,170,178,177,180
13	187,184,185,180,180,178,184,177,188,183
14	188,190,197,184,188,199,184,183,194,193
15	198,202,198,202,198,198,199,198,202,198
16	217,207,207,211,211,202,205,202,204,212
17	213,213,215,213,217,211,216,217,219,209
18	221,219,222,220,214,215,219,214,221,215
19	221,229,225,225,222,236,225,221,227,222
20	230,226,235,230,234,230,229,229,233,234
21	237,237,238,238,238,242,241,231,237,232
22	242,238,241,252,252,242,241,242,242,237
23	256,253,246,255,249,248,252,249,249,256
24	256,257,257,256,259,255,259,256,259,259
25	259,259,262,259,259,258,262,259,259,259

Table A.1: The plume width data collected as part of the data set used to determine the plume width to pulse energy relationship.

Transmission (%)	Pulse Energy (mJ)
1	0.711,0.721,0.724,0.728,0.725,0.727,0.731,0.723,0.726,0.725
2	1.498,1.499,1.506,1.488,1.488,1.487,1.501,1.442,1.507,1.492
3	2.146,2.155,2.166,2.152,2.148,2.166,2.158,2.168,2.167,2.152
4	2.892,2.904,2.889,2.894,2.894,2.896,2.893,2.885,2.894,2.9
5	3.689,3.697,3.696,3.687,3.69,3.705,3.685,3.714,3.698,3.689
6	4.483,4.455,4.476,4.461,4.453,4.448,4.474,4.462,4.461,4.458
7	5.231,5.213,5.238,5.23,5.218,5.224,5.211,5.231,5.221,5.221
8	5.976,5.982,5.967,5.975,5.975,5.999,5.98,5.93,5.954,5.967
9	6.63,6.64,6.64,6.66,6.658,6.742,6.731,6.762,6.785,6.764
10	7.37,7.42,7.42,7.4,7.38,7.41,7.37,7.38,7.38,7.39
11	8.19,8.16,8.19,8.17,8.18,8.17,8.17,8.14,8.17,8.13
12	8.82,8.86,8.86,8.84,8.83,8.84,8.87,8.85,8.84,8.86
13	9.66,9.65,9.69,9.65,9.67,9.66,9.63,9.67,9.63,9.65
14	10.42,10.42,10.4,10.47,10.44,10.44,10.43,10.4,10.44,10.46
15	11.23,11.23,11.28,11.19,11.18,11.22,11.22,11.19,11.21,11.18
16	11.99,12.02,12,12.07,12.02,12.01,12.01,11.96,12,11.99
17	12.86,12.87,12.81,12.85,12.8,12.82,12.79,12.89,12.85,12.8
18	13.57,13.53,13.57,13.6,13.57,13.6,13.54,13.62,13.57,13.61
19	14.35,14.43,14.4,14.38,14.46,14.45,14.47,14.43,14.37,14.39
20	15.15,15.11,15.14,15.09,15.07,15.09,15.14,15.15,15.18,15.15
21	15.86,15.88,15.89,15.92,15.91,15.85,15.85,15.93,15.91,15.93
22	16.67,16.67,16.63,16.71,16.69,16.7,16.68,16.65,16.65,16.69
23	17.4,17.34,17.35,17.33,17.33,17.38,17.37,17.32,17.36,17.32
24	18.11,18.14,18.14,18.22,18.16,18.13,18.09,18.14,18.1,18.2
25	18.86,18.97,18.99,18.98,18.89,18.94,18.88,18.92,18.91,18.89

Table A.2: The pulse energy data collected as part of the data set used to determine the plume width to pulse energy relationship.

Energy (mJ)	Simulated Crater Depth ( $\mu\text{m}$ )
0.5	0
1	0
1.5	0
2	0
2.5	0
3	0
3.5	0
4	0
4.5	0
5	0
5.5	0.013633
6	0.027924
6.5	0.044938
7	0.064073
7.5	0.080477
8	0.099757
8.5	0.118304
9	0.137339
9.5	0.156827
10	0.176568
10.5	0.182461
11	0.208222
11.5	0.23178
12	0.247215
12.5	0.271385
13	0.281985
13.5	0.303946
14	0.32722
14.5	0.346292
15	0.366829
15.5	0.387548
16	0.404496
16.5	0.425978
17	0.440279
17.5	0.463142
18	0.482134
18.5	0.498604
19	0.523667
19.5	0.547465
20	0.566961

Table A.3: The depths of the craters formed in the COMSOL Multiphysics<sup>®</sup> simulation for different energy inputs.

Parameter	Symbol	Value
Molar Mass	$M$	26.98 g
Boiling point	$T_v$	2740 K
Ambient Temperature	$T_{ext}$	293.15 K
Latent Heat of Vaporization	$L_v$	10.53 MJ kg <sup>-1</sup>
Latent Heat of melting	$L_m$	0.39 MJ kg <sup>-1</sup>
Heat of Sublimation	$H_v$	10.92 MJ kg <sup>-1</sup>
Stefan-Boltzmann constant	$\sigma_{sb}$	5.670 374 42e-8 Wm <sup>-2</sup> K <sup>-4</sup>
Resistivity at 20 °C	$\rho_{20}$	3.25e-8 $\Omega$ m
Thermal Coefficient of resistivity	$\gamma$	0.0039 K <sup>-1</sup>
Laser Wavelength	$\lambda$	1064 nm
Pulse full width half maximum	FWHM	9 ns

Table A.4: Parameters used in the COMSOL Multiphysics<sup>®</sup> model.

# References

- [1] F. Emmert-Streib, S. Tripathi, and M. Dehmer, “Analyzing the scholarly literature of digital twin research: Trends, topics and structure,” *IEEE Access*, vol. 11, pp. 69 649–69 666, 2023, this work can be licensed under the Creative Commons Attribution-NonCommercial-NoDerivs 4.0 International license. To view this license visit <https://creativecommons.org/licenses/by-nc-nd/4.0/>. [Online]. Available: <https://doi.org/10.1109/ACCESS.2023.3290488>
- [2] D. Gao, P. Liu, S. Jiang, X. Gao, K. Wang, A. Zhao, and Y. Xue, “Intelligent instrument fault diagnosis and prediction system based on digital twin technology,” *Journal of Physics: Conference Series*, vol. 1983, no. 1, p. 012106, jul 2021, this work is licensed under the Creative Commons Attribution 3.0 Unported license. To view this license visit <http://creativecommons.org/licenses/by/3.0/>. [Online]. Available: <https://dx.doi.org/10.1088/1742-6596/1983/1/012106>
- [3] P. J. Hoffman, E. S. Hopewell, B. Janes, and K. M. Sharp Jr, *Precision machining technology*, 1st ed. Cengage Learning, 2012.
- [4] J. W. Roe, *English and American tool builders*. New York, NY, USA: McGraw-Hill, 1916.
- [5] C. Zhang and J. Yang, *A History of Mechanical Engineering*, 1st ed. Singapore: Springer Singapore, 2020, doi: 10.1007/978-981-15-0833-2\_4. [Online]. Available: [https://doi.org/10.1007/978-981-15-0833-2\\_4](https://doi.org/10.1007/978-981-15-0833-2_4)
- [6] History.com Editors, “Interchangeable Parts,” HISTORY.com <https://www.history.com/topics/inventions/interchangeable-parts> (accessed May 10, 2023).
- [7] B. Carlsson, “The development and use of machine tools in historical perspective,” *Journal of Economic Behavior & Organization*, vol. 5, no. 1, pp. 91–114, 1984, a special Issue on The Dynamics of Market Economies in commemoration of the birth of Joseph A. Schumpeter in 1883. [Online]. Available: <https://www.sciencedirect.com/science/article/pii/0167268184900283>
- [8] L. Wu, J. Leng, and B. Ju, “Digital twins-based smart design and control of ultra-precision machining: A review,” *Symmetry*, vol. 13, no. 9, p. 1717, 2021, doi: 10.3390/sym13091717. [Online]. Available: <https://www.mdpi.com/2073-8994/13/9/1717>
- [9] L. P. Boustan, J. Choi, and D. Clingsmith, “Automation after the assembly line: Computerized machine tools, employment and productivity in the united states,” National Bureau of Economic Research, Tech. Rep., 2022.
- [10] B. R. Barricelli, E. Casiraghi, and D. Fogli, “A survey on digital twin: Definitions, characteristics, applications, and design implications,” *IEEE Access*, vol. 7, pp. 167 653–167 671, 2019, doi: 10.1109/ACCESS.2019.2953499. [Online]. Available: <https://ieeexplore.ieee.org/abstract/document/8901113>
- [11] D. Jones, C. Snider, A. Nassehi, J. Yon, and B. Hicks, “Characterising the digital twin: A systematic literature review,” *CIRP Journal of Manufacturing Science and Technology*, vol. 29, pp. 36–52, 2020, doi: 10.1016/j.cirpj.2020.02.002. [Online]. Available: <https://www.sciencedirect.com/science/article/pii/S1755581720300110>

- [12] U. Dürr, “Laser drilling in industrial use,” *Laser Technik Journal*, vol. 5, no. 3, pp. 57–59, 2008, doi: 10.1002/latj.200890029. [Online]. Available: <https://onlinelibrary.wiley.com/doi/abs/10.1002/latj.200890029>
- [13] C. Wang, Q. Wang, Q. Qian, and B. Di, “The development of laser drilling: A review,” *IOP Conference Series: Materials Science and Engineering*, vol. 782, no. 2, p. 022067, mar 2020, doi: 10.1088/1757-899X/782/2/022067. [Online]. Available: <https://iopscience.iop.org/article/10.1088/1757-899X/782/2/022067>
- [14] C.-P. Wang, K. Erkorkmaz, J. McPhee, and S. Engin, “In-process digital twin estimation for high-performance machine tools with coupled multibody dynamics,” *CIRP Annals*, vol. 69, no. 1, pp. 321–324, 2020, doi: 10.1016/j.cirp.2020.04.047. [Online]. Available: <https://www.sciencedirect.com/science/article/pii/S000785062030069X>
- [15] P. Stavropoulos, A. Papacharalampopoulos, and L. Athanasopoulou, “A molecular dynamics based digital twin for ultrafast laser material removal processes,” *The International Journal of Advanced Manufacturing Technology*, vol. 108, pp. 413–426, 2020, doi: 10.1007/s00170-020-05387-7. [Online]. Available: <https://link.springer.com/article/10.1007/s00170-020-05387-7>
- [16] S. H. Chowdhury, F. Ali, and I. K. Jennions, “A methodology for the experimental validation of an aircraft ecs digital twin targeting system level diagnostics,” in *Annual Conference of the PHM Society*, vol. 11, 2019, pp. 21–26.
- [17] R. Darbali-Zamora, J. Johnson, A. Summers, C. B. Jones, C. Hansen, and C. Showalter, “State estimation-based distributed energy resource optimization for distribution voltage regulation in telemetry-sparse environments using a real-time digital twin,” *Energies*, vol. 14, no. 3, p. 774, 2021, doi: 10.3390/en14030774. [Online]. Available: <https://www.mdpi.com/1996-1073/14/3/774>
- [18] M. Grieves, “Digital twin: manufacturing excellence through virtual factory replication,” *White paper*, vol. 1, no. 2014, pp. 1–7, 2014.
- [19] S. Boschert, C. Heinrich, and R. Rosen, “Next generation digital twin,” in *Proc. tmce*, vol. 2018. Las Palmas de Gran Canaria, Spain, 2018, pp. 7–11.
- [20] J. Vachálek, L. Bartalský, O. Rovný, D. Šišmišová, M. Morhác, and M. Lokšík, “The digital twin of an industrial production line within the industry 4.0 concept,” in *2017 21st international conference on process control (PC)*. IEEE, 2017, pp. 258–262, doi: 10.1109/PC.2017.7976223. [Online]. Available: <https://ieeexplore.ieee.org/document/7976223>
- [21] F. Tao, H. Zhang, A. Liu, and A. Y. Nee, “Digital twin in industry: State-of-the-art,” *IEEE Transactions on industrial informatics*, vol. 15, no. 4, pp. 2405–2415, 2018, doi: 10.1109/TII.2018.2873186. [Online]. Available: <https://ieeexplore.ieee.org/document/8477101>
- [22] C. Semeraro, M. Lezoche, H. Panetto, and M. Dassisti, “Digital twin paradigm: A systematic literature review,” *Computers in Industry*, vol. 130, p. 103469, 2021, doi: 10.1016/j.compind.2021.103469. [Online]. Available: <https://www.sciencedirect.com/science/article/pii/S0166361521000762>
- [23] C. Lo, C. Chen, and R. Y. Zhong, “A review of digital twin in product design and development,” *Advanced Engineering Informatics*, vol. 48, p. 101297, 2021, doi: 10.1016/j.aei.2021.101297. [Online]. Available: <https://www.sciencedirect.com/science/article/pii/S1474034621000513>
- [24] I. Errandonea, S. Beltrán, and S. Arrizabalaga, “Digital twin for maintenance: A literature review,” *Computers in Industry*, vol. 123, p. 103316, 2020, doi: 10.1016/j.compind.2020.103316. [Online]. Available: <https://www.sciencedirect.com/science/article/pii/S0166361520305509>
- [25] T. Bergs, S. Gierlings, T. Auerbach, A. Klink, D. Schraknepper, and T. Augspurger, “The concept of digital twin and digital shadow in manufacturing,” *Procedia CIRP*, vol. 101, pp. 81–84, 2021, doi: 10.1016/j.procir.2021.02.010. [Online]. Available: <https://www.sciencedirect.com/science/article/pii/S2212827121006612>



- [26] K. Židek, J. Pitel', M. Adámek, P. Lazorík, and A. Hošovský, "Digital twin of experimental smart manufacturing assembly system for industry 4.0 concept," *Sustainability*, vol. 12, no. 9, p. 3658, 2020, doi: 10.3390/su12093658. [Online]. Available: <https://www.mdpi.com/2071-1050/12/9/3658>
- [27] A. Detzner, M. Eigner *et al.*, "A digital twin for root cause analysis and product quality monitoring," in *DS 92: Proceedings of the DESIGN 2018 15th International Design Conference*, 2018, pp. 1547–1558, doi: 10.21278/idc.2018.0418.
- [28] N. Metropolis, "The beginning of the monte carlo method," *Los Alamos Science Special Issue*, pp. 125–130, 1987.
- [29] G. E. Moore, "Progress in digital integrated electronics [technical literature, copyright 1975 ieee. reprinted, with permission. technical digest. international electron devices meeting, ieee, 1975, pp. 11-13.]," *IEEE Solid-State Circuits Society Newsletter*, vol. 11, no. 3, pp. 36–37, 2006, doi: 10.1109/NSSC.2006.4804410.
- [30] C. E. Leiserson, N. C. Thompson, J. S. Emer, B. C. Kuszmaul, B. W. Lampson, D. Sanchez, and T. B. Schardl, "There's plenty of room at the top: What will drive computer performance after moore's law?" *Science*, vol. 368, no. 6495, p. eaam9744, 2020, doi: 10.1126/science.aam9744. [Online]. Available: <https://www.science.org/doi/abs/10.1126/science.aam9744>
- [31] T. N. Theis and H.-S. P. Wong, "The end of moore's law: A new beginning for information technology," *Computing in Science & Engineering*, vol. 19, no. 2, pp. 41–50, 2017, doi: 10.1109/MCSE.2017.29. [Online]. Available: <https://ieeexplore.ieee.org/document/7878935>
- [32] R. E. Nance, "Simulation programming languages: an abridged history," in *Winter Simulation Conference Proceedings, 1995*. IEEE, 1995, pp. 1307–1313, doi: 10.1109/WSC.1995.479040.
- [33] S. D. Roberts and D. Pegden, "The history of simulation modeling," in *2017 Winter Simulation Conference (WSC)*. IEEE, 2017, pp. 308–323, doi: 10.1109/WSC.2017.8247795. [Online]. Available: <https://ieeexplore.ieee.org/document/8247795>
- [34] M. Bacic, "On hardware-in-the-loop simulation," in *Proceedings of the 44th IEEE Conference on Decision and Control*. IEEE, 2005, pp. 3194–3198, doi: 10.1109/CDC.2005.1582653. [Online]. Available: <https://ieeexplore.ieee.org/document/1582653>
- [35] C. Dufour, Z. Soghomonian, and W. Li, "Hardware-in-the-loop testing of modern on-board power systems using digital twins," in *2018 International Symposium on Power Electronics, Electrical Drives, Automation and Motion (SPEEDAM)*. IEEE, 2018, pp. 118–123, doi: 10.1109/SPEEDAM.2018.8445302. [Online]. Available: <https://ieeexplore.ieee.org/document/8445302>
- [36] V. Makarov, Y. B. Frolov, I. Parshina, and M. Ushakova, "The design concept of digital twin," in *2019 Twelfth International Conference "Management of large-scale system development" (MLSD)*. IEEE, 2019, pp. 1–4, doi: 10.1109/MLSD.2019.8911091. [Online]. Available: <https://ieeexplore.ieee.org/document/8911091>
- [37] B. Schleich, N. Anwer, L. Mathieu, and S. Wartzack, "Shaping the digital twin for design and production engineering," *CIRP annals*, vol. 66, no. 1, pp. 141–144, 2017. [Online]. Available: <https://doi.org/10.1016/j.cirp.2017.04.040>
- [38] Q. Min, Y. Lu, Z. Liu, C. Su, and B. Wang, "Machine learning based digital twin framework for production optimization in petrochemical industry," *International Journal of Information Management*, vol. 49, pp. 502–519, 2019, doi: 10.1016/j.ijinfomgt.2019.05.020. [Online]. Available: <https://www.sciencedirect.com/science/article/pii/S0268401218311484>
- [39] M. Liu, S. Fang, H. Dong, and C. Xu, "Review of digital twin about concepts, technologies, and industrial applications," *Journal of Manufacturing Systems*, vol. 58, pp. 346–361, 2021, digital Twin towards Smart Manufacturing and Industry 4.0. [Online]. Available: <https://www.sciencedirect.com/science/article/pii/S0278612520301072>

- [40] J. Trauer, S. Schweigert-Recksiek, C. Engel, K. Spreitzer, and M. Zimmermann, “What is a digital twin?—definitions and insights from an industrial case study in technical product development,” in *Proceedings of the Design Society: DESIGN Conference*, vol. 1. Cambridge University Press, 2020, pp. 757–766, doi: 10.1017/dsd.2020.15.
- [41] Z. Zhaoyun and L. Linjun, “Application status and prospects of digital twin technology in distribution grid,” *Energy Reports*, vol. 8, pp. 14170–14182, 2022, doi: 10.1016/j.egy.2022.10.410. [Online]. Available: <https://www.sciencedirect.com/science/article/pii/S2352484722023459>
- [42] V. Gattulli, F. Franchi, F. Graziosi, A. Marotta, C. Rinaldi, F. Potenza, and U. D. Sabatino, “Design and evaluation of 5g-based architecture supporting data-driven digital twins updating and matching in seismic monitoring,” *Bulletin of Earthquake Engineering*, vol. 20, no. 9, pp. 4345–4365, July 2022, doi: 10.1007/s10518-022-01329-8. [Online]. Available: <https://link.springer.com/article/10.1007/s10518-022-01329-8>
- [43] R. Dangi, P. Lalwani, G. Choudhary, I. You, and G. Pau, “Study and investigation on 5g technology: A systematic review,” *Sensors*, vol. 22, no. 1, p. 26, 2022, doi: 10.3390/s22010026. [Online]. Available: <https://www.mdpi.com/1424-8220/22/1/26>
- [44] D. Miljković, “Fault detection methods: A literature survey,” in *2011 Proceedings of the 34th international convention MIPRO*. IEEE, 2011, pp. 750–755. [Online]. Available: <https://ieeexplore.ieee.org/document/5967153>
- [45] A. Papacharalamopoulos, C. Giannoulis, P. Stavropoulos, and D. Mourtzis, “A digital twin for automated root-cause search of production alarms based on kpis aggregated from iot,” *Applied Sciences*, vol. 10, no. 7, p. 2377, 2020, doi: 10.3390/app10072377. [Online]. Available: <https://www.mdpi.com/2076-3417/10/7/2377>
- [46] D. Wang, Z. Zhang, M. Zhang, M. Fu, J. Li, S. Cai, C. Zhang, and X. Chen, “The role of digital twin in optical communication: fault management, hardware configuration, and transmission simulation,” *IEEE Communications Magazine*, vol. 59, no. 1, pp. 133–139, 2021, doi: 10.1109/MCOM.001.2000727. [Online]. Available: <https://ieeexplore.ieee.org/document/9356524>
- [47] H. Darvishi, D. Ciunzo, E. R. Eide, and P. S. Rossi, “Sensor-fault detection, isolation and accommodation for digital twins via modular data-driven architecture,” *IEEE Sensors Journal*, vol. 21, no. 4, pp. 4827–4838, 2020, doi: 10.1109/JSEN.2020.3029459. [Online]. Available: <https://ieeexplore.ieee.org/document/9216114>
- [48] K. Rose, S. Eldridge, and L. Chapin, “The internet of things: An overview,” *The internet society (ISOC)*, vol. 80, pp. 1–50, 2015.
- [49] R. Van Kranenburg, “The internet of things,” *World Affairs: The Journal of International Issues*, vol. 15, no. 4, pp. 126–141, 2011. [Online]. Available: <https://www.jstor.org/stable/48505085>
- [50] T. H. Luan, R. Liu, L. Gao, R. Li, and H. Zhou, “The paradigm of digital twin communications,” *arXiv preprint arXiv:2105.07182*, 2021, doi: 10.48550/arXiv.2105.07182.
- [51] Y. Liu, L. Zhang, Y. Yang, L. Zhou, L. Ren, F. Wang, R. Liu, Z. Pang, and M. J. Deen, “A novel cloud-based framework for the elderly healthcare services using digital twin,” *IEEE access*, vol. 7, pp. 49088–49101, 2019, doi: 10.1109/ACCESS.2019.2909828. [Online]. Available: <https://ieeexplore.ieee.org/document/8686260>
- [52] K. N. Qureshi, A. H. Abdullah, and R. W. Anwar, “The evolution in health care with information and communication technologies,” in *Proceeding of 2nd International Conference of Applied Information and Communications Technology-2014*. Elsevier, 2014.
- [53] J. I. Jimenez, H. Jahankhani, and S. Kendzierskyj, *Health Care in the Cyberspace: Medical Cyber-Physical System and Digital Twin Challenges*. Cham: Springer International Publishing, 2020, pp. 79–92, doi: 10.1007/978-3-030-18732-3\_6. [Online]. Available: [https://doi.org/10.1007/978-3-030-18732-3\\_6](https://doi.org/10.1007/978-3-030-18732-3_6)

- [54] B. Grosman, A. Roy, D. Wu, N. Parikh, L. J. Lintereur, N. Schneider, R. L. Brazg, S. K. Garg, and R. Vigersky, “1006-P: Personalized Hybrid Closed-Loop Therapy Using a Digital Twin in Patients with Type 1 Diabetes: At-Home Data,” *Diabetes*, vol. 69, no. Supplement\_1, 06 2020, 1006-P. [Online]. Available: <https://doi.org/10.2337/db20-1006-P>
- [55] K. Y. H. Lim, P. Zheng, and C.-H. Chen, “A state-of-the-art survey of digital twin: techniques, engineering product lifecycle management and business innovation perspectives,” *Journal of Intelligent Manufacturing*, vol. 31, no. 6, pp. 1313–1337, 2020.
- [56] J. Guo, N. Zhao, L. Sun, and S. Zhang, “Modular based flexible digital twin for factory design,” *Journal of Ambient Intelligence and Humanized Computing*, vol. 10, no. 3, pp. 1189–1200, 2019, doi: 10.1007/s12652-018-0953-6. [Online]. Available: <https://doi.org/10.1007/s12652-018-0953-6>
- [57] W. Luo, T. Hu, C. Zhang, and Y. Wei, “Digital twin for cnc machine tool: modeling and using strategy,” *Journal of Ambient Intelligence and Humanized Computing*, vol. 10, no. 3, pp. 1129–1140, 2019, doi: 10.1007/s12652-018-0946-5. [Online]. Available: <https://doi.org/10.1007/s12652-018-0946-5>
- [58] D. Guo, R. Y. Zhong, P. Lin, Z. Lyu, Y. Rong, and G. Q. Huang, “Digital twin-enabled graduation intelligent manufacturing system for fixed-position assembly islands,” *Robotics and Computer-Integrated Manufacturing*, vol. 63, p. 101917, 2020, doi: 10.1016/j.rcim.2019.101917. [Online]. Available: <https://www.sciencedirect.com/science/article/pii/S0736584519304405>
- [59] T. H.-J. Uhlemann, C. Schock, C. Lehmann, S. Freiburger, and R. Steinhilper, “The digital twin: demonstrating the potential of real time data acquisition in production systems,” *Procedia Manufacturing*, vol. 9, pp. 113–120, 2017, doi: 10.1016/j.promfg.2017.04.043. [Online]. Available: <https://www.sciencedirect.com/science/article/pii/S2351978917301610>
- [60] J. Bao, D. Guo, J. Li, and J. Zhang, “The modelling and operations for the digital twin in the context of manufacturing,” *Enterprise Information Systems*, vol. 13, no. 4, pp. 534–556, 2019, doi: 10.1080/17517575.2018.1526324.
- [61] X. Xie, Q. Lu, A. K. Parlikad, and J. M. Schooling, “Digital twin enabled asset anomaly detection for building facility management,” *IFAC-PapersOnLine*, vol. 53, no. 3, pp. 380–385, 2020, doi: 10.1016/j.ifacol.2020.11.061. [Online]. Available: <https://www.sciencedirect.com/science/article/pii/S2405896320302111>
- [62] G. P. Lydon, S. Caranovic, I. Hischier, and A. Schlueter, “Coupled simulation of thermally active building systems to support a digital twin,” *Energy and Buildings*, vol. 202, p. 109298, 2019, doi: 10.1016/j.enbuild.2019.07.015. [Online]. Available: <https://www.sciencedirect.com/science/article/pii/S0378778819305201>
- [63] A. Fuller, Z. Fan, C. Day, and C. Barlow, “Digital twin: Enabling technologies, challenges and open research,” *IEEE access*, vol. 8, pp. 108 952–108 971, 2020, doi: 10.1109/ACCESS.2020.2998358. [Online]. Available: <https://ieeexplore.ieee.org/document/9103025>
- [64] J. Jang-Jaccard and S. Nepal, “A survey of emerging threats in cybersecurity,” *Journal of Computer and System Sciences*, vol. 80, no. 5, pp. 973–993, 2014, doi: 10.1016/j.jcss.2014.02.005. [Online]. Available: <https://www.sciencedirect.com/science/article/pii/S0022000014000178>
- [65] J. Lapienyte. “Siemens Metaverse exposes sensitive corporate data”. Cybernews. <https://cybernews.com/security/siemens-metaverse-data-leak/> (accessed Oct. 29, 2023).
- [66] K. Shah, T. V. Prabhakar, S. C. R., A. S. V., and V. K. T, “Construction of a digital twin framework using free and open-source software programs,” *IEEE Internet Computing*, vol. 26, no. 5, pp. 50–59, 2022, doi: 10.1109/MIC.2021.3051798. [Online]. Available: <https://ieeexplore.ieee.org/document/9325003>

- [67] P. Milonni and J. Eberly, *Laser Physics*. Hoboken, NJ, USA: John Wiley & Sons, Ltd, 2010, doi: 10.1002/9780470409718. [Online]. Available: <https://onlinelibrary.wiley.com/doi/abs/10.1002/9780470409718>
- [68] D. Williams, “Laser basics,” *Anaesthesia & Intensive Care Medicine*, vol. 9, no. 12, pp. 550–552, 2008, doi: 10.1016/j.mpaic.2008.09.008. [Online]. Available: <https://www.sciencedirect.com/science/article/pii/S1472029908002191>
- [69] W. Silfvast, *Laser Fundamentals*, 2nd ed. Cambridge, UK: Cambridge University Press, 2004, doi: 10.1017/CBO9780511616426.003.
- [70] S. A. Payne and G. F. Albrecht, “Lasers, solid-state,” in *Encyclopedia of Physical Science and Technology*, 3rd ed., R. A. Meyers, Ed. New York: Academic Press, 2003, pp. 477–498, doi: 10.1016/B0-12-227410-5/00372-0. [Online]. Available: <https://www.sciencedirect.com/science/article/pii/B0122274105003720>
- [71] V. Lupei and A. Lupei, “Nd:yag at its 50th anniversary: Still to learn,” *Journal of Luminescence*, vol. 169, pp. 426–439, 2016, the 17th International Conference on Luminescence and Optical Spectroscopy of Condensed Matter (ICL’14). [Online]. Available: <https://www.sciencedirect.com/science/article/pii/S0022231315002094>
- [72] D. Franta and M.-G. Mureşan, “Wide spectral range optical characterization of yttrium aluminum garnet (yag) single crystal by the universal dispersion model,” *Opt. Mater. Express*, vol. 11, no. 12, pp. 3930–3945, Dec 2021, doi: 10.1364/OME.441088. [Online]. Available: <https://opg.optica.org/ome/abstract.cfm?URI=ome-11-12-3930>
- [73] Y. Nagata, R. Takeda, and M. Suginome, “High-pressure circular dichroism spectroscopy up to 400 mpa using polycrystalline yttrium aluminum garnet (yag) as pressure-resistant optical windows,” *RSC Adv.*, vol. 6, pp. 109 726–109 729, 2016, doi: 10.1039/C6RA23736C. [Online]. Available: <http://dx.doi.org/10.1039/C6RA23736C>
- [74] S. Kostić, Z. Lazarević, V. Radojević, A. Milutinović, M. Romčević, N. Romčević, and A. Valčić, “Study of structural and optical properties of yag and nd:yag single crystals,” *Materials Research Bulletin*, vol. 63, pp. 80–87, 2015, doi: 10.1016/j.materresbull.2014.11.033. [Online]. Available: <https://www.sciencedirect.com/science/article/pii/S0025540814007144>
- [75] J. Hecht, “A short history of laser development,” *Applied optics*, vol. 49, no. 25, pp. F99–F122, 2010, doi: 10.1117/1.3483597. [Online]. Available: <https://doi.org/10.1117/1.3483597>
- [76] B. L. Garrec, “Laser-diode and Flash Lamp Pumped Solid-State Lasers,” *AIP Conference Proceedings*, vol. 1228, no. 1, pp. 111–116, 04 2010, doi: 10.1063/1.3426039. [Online]. Available: <https://doi.org/10.1063/1.3426039>
- [77] W. Koechner, *Q-Switching*. New York, NY: Springer New York, 2006, pp. 488–533, doi: 10.1007/0-387-29338-8\_9. [Online]. Available: [https://doi.org/10.1007/0-387-29338-8\\_9](https://doi.org/10.1007/0-387-29338-8_9)
- [78] R. E. Russo, X. Mao, J. Yoo, and J. Gonzalez, “Chapter 3 - laser ablation,” in *Laser-Induced Breakdown Spectroscopy*, 2nd ed., J. P. Singh and S. N. Thakur, Eds. Amsterdam: Elsevier, 2007, pp. 41–70, doi: 10.1016/B978-0-12-818829-3.00003-4. [Online]. Available: <https://www.sciencedirect.com/science/article/pii/B9780128188293000034>
- [79] L. Canguero, T. Le Quang, and R. Vilar, “8 - laser surface modification of biological hard tissues,” in *Laser Surface Modification of Biomaterials*, R. Vilar, Ed. Woodhead Publishing, 2016, pp. 221–251, doi: 10.1016/B978-0-08-100883-6.00008-3. [Online]. Available: <https://www.sciencedirect.com/science/article/pii/B9780081008836000083>
- [80] A. Bogaerts, Z. Chen, R. Gijbels, and A. Vertes, “Laser ablation for analytical sampling: what can we learn from modeling?” *Spectrochimica Acta Part B: Atomic Spectroscopy*, vol. 58, no. 11, pp. 1867–1893, 2003, doi: 10.1016/j.sab.2003.08.004. [Online]. Available: <https://www.sciencedirect.com/science/article/pii/S0584854703001666>

- [81] N. Arnold, J. Gruber, and J. Heitz, “Spherical expansion of the vapor plume into ambient gas: an analytical model,” *Applied Physics A*, vol. 69, pp. S87–S93, 1999, doi: 10.1007/s003399900183. [Online]. Available: <https://doi.org/10.1007/s003399900183>
- [82] M. Predteceensky and A. Mayorov, “Expansion of laser plasma in oxygen at laser deposition of htsc films: theoretical model,” *Applied Superconductivity*, vol. 1, no. 10, pp. 2011–2017, 1993, world Congress on Superconductivity Proceedings of the 3rd International Conference and Exhibition. [Online]. Available: <https://www.sciencedirect.com/science/article/pii/0964180793903497>
- [83] S. Amoruso, J. Schou, and J. G. Lunney, “Energy balance of a laser ablation plume expanding in a background gas,” *Applied Physics A*, vol. 101, no. 1, pp. 209–214, 2010, doi: 10.1007/s00339-010-5753-6. [Online]. Available: <https://doi.org/10.1007/s00339-010-5753-6>
- [84] W. J. Keller, N. Shen, A. M. Rubenchik, S. Ly, R. Negres, R. N. Raman, J.-H. Yoo, G. Guss, J. S. Stolken, M. J. Matthews *et al.*, “Physics of picosecond pulse laser ablation,” *Journal of Applied Physics*, vol. 125, no. 8, p. 085103, 2019, doi: 10.1063/1.5080628. [Online]. Available: <https://doi.org/10.1063/1.5080628>
- [85] B. Christensen, K. Vestentoft, and P. Balling, “Short-pulse ablation rates and the two-temperature model,” *Applied Surface Science*, vol. 253, no. 15, pp. 6347–6352, 2007, proceedings of the Fifth International Conference on Photo-Excited Processes and Applications. [Online]. Available: <https://www.sciencedirect.com/science/article/pii/S0169433207001092>
- [86] J. Byskov-Nielsen, J.-M. Savolainen, M. S. Christensen, and P. Balling, “Ultra-short pulse laser ablation of copper, silver and tungsten: experimental data and two-temperature model simulations,” *Applied Physics A*, vol. 103, no. 2, pp. 447–453, 2011, doi: 10.1007/s00339-011-6363-7. [Online]. Available: <https://doi.org/10.1007/s00339-011-6363-7>
- [87] C. Chen, F. Zhang, Y. Zhang, X. Xiong, B.-F. Ju, H. Cui, and Y.-L. Chen, “Single-pulse femtosecond laser ablation of monocrystalline silicon: A modeling and experimental study,” *Applied Surface Science*, vol. 576, p. 151722, 2022, doi: 10.1016/j.apsusc.2021.151722. [Online]. Available: <https://www.sciencedirect.com/science/article/pii/S0169433221027665>
- [88] M. Dal, L. Carvalho, A. Semerok, W. Pacquentin, and H. Maskrot, “Simulation of bi-material nanosecond laser ablation,” in *Proc. COMSOL Conference 2019*. COMSOL, Inc., September 2019.
- [89] M. J. Matthews, “Simulating laser-material interactions,” *Laser Focus World*, vol. 51, no. 8, 8 2015. [Online]. Available: <https://www.osti.gov/biblio/1772304>
- [90] J. Radice, P. Joyce, A. Tresansky, and R. Watkins, “A comsol model of damage evolution due to high energy laser irradiation of partially absorptive materials,” in *Proc. COMSOL Conference 2012*. Boston, MA, USA: COMSOL, Inc., October 2012.
- [91] R. A. Mitchell, D. W. Schumacher, and E. A. Chowdhury, “Modeling crater formation in femtosecond-pulse laser damage from basic principles,” *Optics Letters*, vol. 40, no. 10, pp. 2189–2192, 2015, doi: 10.1364/OL.40.002189. [Online]. Available: <https://opg.optica.org/ol/abstract.cfm?URI=ol-40-10-2189>
- [92] Z. Zhang, Q. Nian, C. C. Dumanidis, and Y. Liao, “First-principles modeling of laser-matter interaction and plasma dynamics in nanosecond pulsed laser shock processing,” *Journal of Applied Physics*, vol. 123, no. 5, p. 054901, 2018, doi: 10.1063/1.5021894. [Online]. Available: <https://doi.org/10.1063/1.5021894>
- [93] S. Sonntag, C. Trichet Paredes, J. Roth, and H.-R. Trebin, “Molecular dynamics simulations of cluster distribution from femtosecond laser ablation in aluminum,” *Applied Physics A*, vol. 104, pp. 559–565, 2011, doi: 10.1007/s00339-011-6460-7. [Online]. Available: <https://doi.org/10.1007/s00339-011-6460-7>

- [94] S. Tani and Y. Kobayashi, “Ultrafast laser ablation simulator using deep neural networks,” *Scientific Reports*, vol. 12, no. 1, p. 5837, 2022, doi: 10.1038/s41598-022-09870-x. [Online]. Available: <https://doi.org/10.1038/s41598-022-09870-x>
- [95] C. Lu, J. Fei, X. Meng, Y. Li, and Z. Liu, “Thermal error prediction and compensation of digital twin laser cutting based on t-xgboost,” *Sensors*, vol. 22, no. 18, p. 7022, 2022, doi: 10.3390/s22187022. [Online]. Available: <https://www.mdpi.com/1424-8220/22/18/7022>
- [96] S. Tani and Y. Kobayashi, “Pulse-by-pulse depth profile measurement of femtosecond laser ablation on copper,” *Applied Physics A*, vol. 124, pp. 1–5, 02 2018, doi: 10.1007/s00339-018-1694-2. [Online]. Available: <https://doi.org/10.1007/s00339-018-1694-2>
- [97] A. H. Naronikar, H. A. Jamadagni, A. Simha, and B. Saikiran, “Optimizing the heat treatment parameters of al-6061 required for better formability,” *Materials Today: Proceedings*, vol. 5, no. 11, Part 3, pp. 24 240–24 247, 2018, doi: 10.1016/j.matpr.2018.10.219. [Online]. Available: <https://www.sciencedirect.com/science/article/pii/S2214785318325148>
- [98] C. Yeo, S. Tam, S. Jana, and M. W. Lau, “A technical review of the laser drilling of aerospace materials,” *Journal of Materials Processing Technology*, vol. 42, no. 1, pp. 15–49, 1994, doi: 10.1016/0924-0136(94)90073-6. [Online]. Available: <https://www.sciencedirect.com/science/article/pii/0924013694900736>
- [99] J. Gao, Y. Cao, L. Lu, Z. Hu, K. Wang, F. Guo, and Y. Yan, “Study on the interaction between nanosecond laser and 6061 aluminum alloy considering temperature dependence,” *Journal of Alloys and Compounds*, vol. 892, p. 162044, 2022, doi: 10.1016/j.jallcom.2021.162044. [Online]. Available: <https://www.sciencedirect.com/science/article/pii/S0925838821034538>
- [100] W. Frei. “Modeling Thermal Ablation for Material Removal”. COMSOL Blog. <https://www.comsol.com/blogs/modeling-thermal-ablation-for-material-removal/> (accessed Jan. 15, 2023).
- [101] Y. Wang, N. Shen, G. K. Befekadu, and C. L. Pasiliao, “Modeling pulsed laser ablation of aluminum with finite element analysis considering material moving front,” *International Journal of Heat and Mass Transfer*, vol. 113, pp. 1246–1253, 2017, doi: 10.1016/j.ijheatmasstransfer.2017.06.056. [Online]. Available: <https://www.sciencedirect.com/science/article/pii/S0017931017309675>
- [102] Y. Zhang, D. Zhang, J. Wu, Z. He, and X. Deng, “A thermal model for nanosecond pulsed laser ablation of aluminum,” *AIP Advances*, vol. 7, no. 7, p. 075010, 07 2017, doi: 10.1063/1.4995972. [Online]. Available: <https://doi.org/10.1063/1.4995972>
- [103] M. Stafe, C. Negutu, and I. M. Popescu, “Theoretical determination of the ablation rate of metals in multiple-nanosecond laser pulses irradiation regime,” *Applied Surface Science*, vol. 253, no. 15, pp. 6353–6358, 2007, proceedings of the Fifth International Conference on Photo-Excited Processes and Applications. [Online]. Available: <https://www.sciencedirect.com/science/article/pii/S0169433207001079>
- [104] F. Rubbi, X. Zhang, F. Delzendehrooy, B. Mao, Q. Nian, C. C. Dumanidis, and Y. Liao, “Chemical etching enhanced nanosecond pulsed laser micromachining: An experimental and numerical investigation,” *Journal of Manufacturing Processes*, vol. 108, pp. 384–394, 2023, doi: 10.1016/j.jmapro.2023.11.017. [Online]. Available: <https://www.sciencedirect.com/science/article/pii/S1526612523010575>
- [105] E. Chevallier, V. Bruyère, and P. Namy. (2018). Finite element prediction of laser-material interaction using COMSOL Multiphysics® [PDF Document]. Available: [https://www.comsol.com/paper/download/566582/chevallier\\_presentation.pdf](https://www.comsol.com/paper/download/566582/chevallier_presentation.pdf)